

**HIGH INTENSITY
X-RAY CHARACTERIZATION STRATEGIES
FOR EVALUATING NANOMATERIALS**

THESIS

**Presented to the Graduate Council of
Texas State University-San Marcos
in Partial Fulfillment of
the Requirements**

For the Degree

Master of SCIENCE

By

Shannon G. Fritz, B.A.

**San Marcos, Texas
December 2003**

COPYRIGHT

by

Shannon Gail Fritz

2003

This thesis is dedicated to my parents,
Auntie, and Naw-Nee,
for their love and for believing in me.

ACKNOWLEDGEMENTS

The research presented in this thesis was made possible by the collaboration of many people. I would like to acknowledge Daniel Chesire, Sailesh Merchant, and Max Lippitt of Agere Systems in Orlando, Florida for providing cobalt silicide films as well as useful feedback in the analysis of these films.

I would also like to thank Dennis Eberl and David Rutherford for performing gas absorption analysis on the nanopowders I analyzed, as well as technical support with the MudMaster program.

I would especially like to thank my thesis committee; Dr. Wilhelmus Geerts for his enthusiastic approach to physics, Dr. Heather Galloway for her insight and direction, and my advisor, Dr. Carlos Gutierrez for his support and encouragement as professor, employer, and mentor over the last few years.

I also want to thank the other students in my research group, Dr. Anup Bandyopadhyay, Dana Larison, Steven Rios, Jesse Contreras, Jonathan Garcia, and Casey Smith, for their support and feedback.

TABLE OF CONTENTS

ACKNOWLEDGEMENTS.....	v
LIST OF TABLES.....	vii
LIST OF FIGURES.....	viii
INTRODUCTION.....	1
1.1 USING X-RAYS FOR EXPERIMENTAL ANALYSIS.....	1
1.2 UNIQUE PROPERTIES OF NANOPOWDERS.....	2
1.3 IMPORTANCE OF COSI_2 IN SUBMICRON IC TECHNOLOGY.....	3
BACKGROUND.....	4
2.1 X-RADIATION AND AN IMPROVED OPTICAL SYSTEM.....	4
2.2 OPTICS.....	7
2.1.1 ABSORPTION.....	9
2.1.2 FILTRATION.....	11
2.1.3 CRYSTAL DIFFRACTION.....	12
2.1.4 COLLIMATE AND FOCUS.....	14
2.2 NANOPOWDER PARTICLE SIZE AND STRAIN DETERMINATION THEORY.....	17
2.3 COBALT SILICIDES FOR ULTRA LARGE SCALE INTEGRATION.....	20
DATA & ANALYSIS.....	22
3.1 POWDER X-RAY DIFFRACTION PATTERNS.....	22
3.1.1 LaB_6 STANDARD CALIBRATION.....	24
3.1.2 PARTICLE SIZE AND STRAIN DETERMINATION FOR MgO NANOPOWDER.....	27
3.1.3 TEM.....	29
3.2 COSI_2 DIFFRACTION PATTERNS.....	32
3.2.1 ATOMIC FORCE MICROSCOPY FOR SURFACE ROUGHNESS ANALYSIS.....	32
3.2.2 PBXRD, HAXRD, AND XRR.....	34
3.2.3 REFS MERCURY DATA FITTING.....	39
3.2.4 VSM MEASUREMENTS.....	42
CONCLUSION.....	44
APPENDIX A.....	46
APPENDIX B.....	48
BIBLIOGRAPHY.....	50
VITA.....	52

LIST OF TABLES

Table 1: <i>Average particle and crystallite size of MgO nanopowder as given by manufacturer. Particles consist of individual crystallites.</i>	22
Table 2: <i>Diffraction peak values used for Williamson-Hall plot.</i>	23
Table 3: <i>Comparison of three methods of size determination; Scherrer, Eq. 2.16, Williamson-Hall Plot, Fig. 13, and MudMaster.</i>	28
Table 4: <i>Comparison of AFM vs. REFS computer modeling surface roughness</i>	39

LIST OF FIGURES

Figure 1: <i>Relationship of sheet resistance to film thickness.</i>	3
Figure 2: <i>Electron states of a barium atom; if an incident electron accelerating toward the atom has sufficient energy to eject an electron from a lower energy state, the atom will be left in an excited state. The atom can reduce its energy by emitting an electron from a higher state to produce an x-ray photon. (Wittke)</i>	4
Figure 3: <i>(a) Schematic of using graphite crystal previously to produce monochromatic x-ray beam. (b) The multilayer optics produces a more intense beam.</i>	8
Figure 4: <i>(a) Schematics of optics in path of incident beam, (b) actual optics, and position of optics in BEDE D1 X-Ray Diffractometer.</i>	9
Figure 5: <i>Comparison of the spectra of Cu radiation (a) before and (b) after passage through a nickel filter. The dashed line is the mass absorption coefficient of Ni. (Cullity⁴)</i>	12
Figure 6: <i>Crystallographic planes reflecting x-rays. (Jenkins³)</i>	13
Figure 7: <i>Unit cells consists of a set of parallel planes which have different orientations depending on the structure of the unit cell (Lattman).</i>	14
Figure 8: <i>Schematic of nickel-carbon interface at surface of mirror</i>	15
Figure 9: <i>A ray bundle reflected on a parabola. F is the focus, A1 and A2 are the incidence points, and f_1 and f_2 are focal lengths. Θ_p is the incidence/reflection angle. $\Delta\theta_p$ is the opening and Δy is the width of the parallel ray bundle. (Schuster⁶)</i>	16
Figure 10: <i>Comparison of XRD data for three different grain sizes of MgO. (Sample numbers correspond to sizes given in Table 1.) Additional peaks seen for the smaller sizes may actually be due to that size's affinity for reacting with water in the atmosphere.</i>	24
Figure 11: <i>HAXRD of LaB6 Standard Reference Material; peak broadening is due only to instrumentation</i>	25
Figure 12: <i>Least fit polynomial curve of FWHM vs. 2Theta-Omega for LaB6 standard.</i>	26
Figure 13: <i>Williamson-Hall plot for size and strain determination for varying MgO sample sizes. The calculated values of 92.5, 39.2, and 4.7 nm correspond to manufacturer sizes of 100 nm, 36 nm, and NanoActiveTM respectively. The strain for the NanoActiveTM material is greater than that of the other two made by Nanostructured & Amorphous Materials, Inc and it is unclear whether this is a function of the size difference or the manufacturing process, for which neither company would give information.</i>	26
Figure 14: <i>Schematic of transmission electron microscope, TEM. Electrons are produced by the electron gun and focused onto the sample by two condenser lenses. The interaction of the electrons as they pass through the sample form an image. Areas of the sample that are very electron dense will appear darker than areas which are not and allow electrons to pass through with little or no interaction. (Koke)</i>	29

Figure 15: TEM images of MgO prepared on Formvar®-coated copper grids; (a) NanoActive™, (b) 36 nm, (c) 100 nm.....	31
Figure 16: AFM data for 400 Å wafers, including bare Si reference	33
Figure 17: PBXRD scans for (a) as-deposited cobalt, (b) RTA1, (c) RTA1/strip, (d) RTA1/strip/RTA2. The scans reveal a more textured film after annealing than the as-deposited cobalt film, as well as the formation of CoSi and CoSi ₂ after the first and second anneal, respectively.	36
Figure 18: HAXRD scans for (a) as-deposited cobalt, (b) RTA1, (c) RTA1/strip, (d) RTA1/strip/RTA2. The scans show a highly ordered as-deposited cobalt film, and a tendency toward disorder after annealing as well as the formation of CoSi and CoSi ₂ after the first and second anneal, respectively.....	37
Figure 19: XRR scan sfor (a) as-deposited cobalt, (b) RTA1, (c) RTA1/strip, (d) RTA1/strip/RTA2. The scans show the roughness of the film increases with annealing as verified by AFM. The data fits also reveal the formation of CoSi and CoSi ₂ after the first and second anneal, respectively.	38
Figure 20: REFS computer modeling for 100ÅCo (a) as-deposited Co, (b) RTA1, (c) RTA1/strip, (d) RTA2.	40
Figure 21: REFS computer modeling for 100ÅCo/90ÅTi (a) RTA1, (b) RTA1/strip, (c) RTA2	41
Figure 22: VSM data for 100 Å and 400 Å cobalt on silicon as well as 50 Å Ti/500 Å Co on 5000 Å Si; shows initial cobalt film to be ferromagnetic. After annealing, no hysteresis is seen (not shown).	43

CHAPTER 1

INTRODUCTION

1.1 USING X-RAYS FOR EXPERIMENTAL ANALYSIS

The human eye can resolve objects as small as 0.2 mm apart. This limit generates the need for microscopes, some of which are able to resolve down to atomic sizes such as scanning tunneling and atomic force microscopes. However, the microscope is only useful for surface analysis. To see inside an object, it is necessary to somehow break it apart, often destroying it. X-rays can reveal information about an object in the same way light rays create an image for our eyes, depending on how the x-rays interact with the object. However, X-rays are able to penetrate an object much deeper than visible light and react by being absorbed, reflected, or transmitted. The information can then be analyzed to determine the elemental composition of the material and properties such as thickness and crystal structure.

With the recent advances made in the area of nanotechnology, the need to characterize submicron materials has become increasingly important. Materials at this size may behave very differently than the same material in bulk sizes, creating infinite possibilities for applications in electronics, medicine, and other disciplines. The X-rays along with other types of analysis can be used in conjunction with one another to ensure as much is understood about new materials as possible.

The x-ray data for this thesis was obtained using a BEDE D1 X-Ray Diffractometer (XRD). Materials analyzed include MgO nanopowders ranging in particle sizes from 5 to 100 nm and cobalt thin films with thicknesses of 100 and 400 Å on silicon. The diffraction patterns obtained from the nanopowder material were analyzed to obtain information about particle size and strain. The cobalt films were analyzed to determine crystal structure before and after annealing, as well as thickness of the film and roughness of the surface and interfaces.

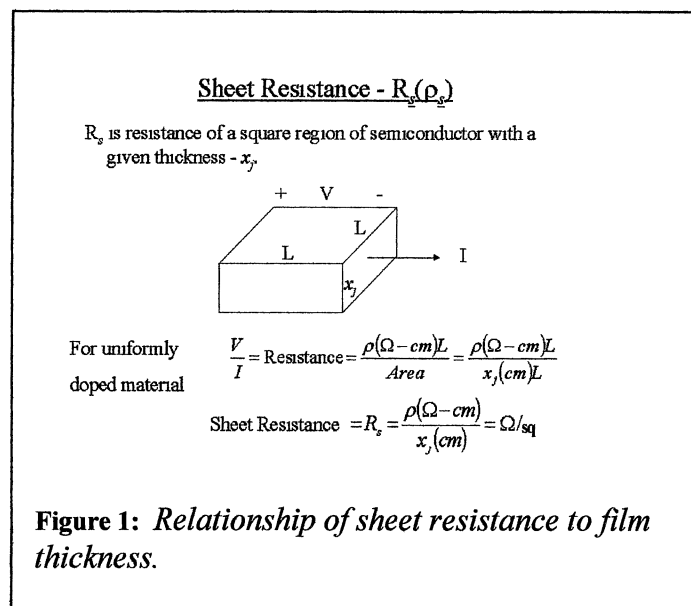
1.2 UNIQUE PROPERTIES OF NANOPOWDERS

The term nanostructure refers to materials that have one or more dimensions on the order of nanometers. Recently attention has been given to the nanoscale region as a new and exciting area of material science with numerous applications. Much research is currently being done to describe particles of this size. This task has proven challenging in that the nanometer size particles behave differently from their bulk-size counterparts. As the size of the particles decrease, the physical properties of the materials change dramatically. This arises from the fact that the size is now similar to physical quantities such as “grain size, magnetic domain size, elastic or inelastic scattering length of conduction electrons, wavelength of excitations such as phonons or magnons, De Broglie wavelength of the electron, phase-coherence length in a semiconductor, etc.”(Jongh¹) These changes can affect the electronic, magnetic, and optical characteristics of the material as well as its reaction to other materials. The large surface area to volume ratio may also increase the hardness of the material, causing it to be more stable than a bulk material. Since the properties of the material are extremely size-dependent, size analysis

is imperative. This thesis discusses some of the theory of determining size using x-ray analysis and gives data to support this theory.

1.3 IMPORTANCE OF CoSi_2 IN SUBMICRON IC TECHNOLOGY

Integrated circuits (IC) are also decreasing in size, creating challenges for the semiconductor industry. The reduction of source/drain area, junction depth, and contact size results in high sheet (R_s) and contact (R_c) resistances. Fig. 1. shows the relationship of sheet resistance to film thickness. R_s is inversely proportional to thickness, limiting the size of the device beyond submicron thicknesses. These high resistances degrade the ability of the transistor to drive current and cause the device to fail to work properly. The solution has been to create silicides, compounds of silicon, with lower R_s and R_c to improve the device performance. CoSi_2 is beginning to replace TiSi_2 because the sheet resistance of cobalt is not affected by decreasing linewidth. This thesis will research the best method of CoSi_2 fabrication on silicon wafers.



CHAPTER 2
BACKGROUND

2.1 X-RADIATION AND AN IMPROVED OPTICAL SYSTEM

X-rays are essentially electromagnetic radiation much like visible light in that they consist of both magnetic and electric fields oscillating perpendicular to one another, but with a wavelength on the order of 10^{-8} m, anywhere from 0.5 to 2.5 Å. The magnetic field will interact only with other magnetic fields and does not factor much in x-ray interaction with matter. The electric field of an x-ray will cause electrons surrounding an atom to accelerate and decelerate. The extra energy that the affected electron gains must

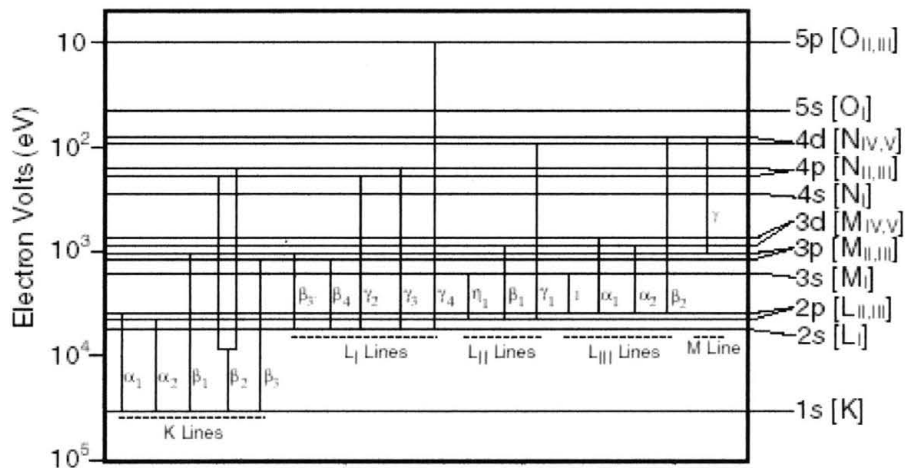


Figure 2: *Electron states of a barium atom; if an incident electron accelerating toward the atom has sufficient energy to eject an electron from a lower energy state, the atom will be left in an excited state. The atom can reduce its energy by emitting an electron from a higher state to produce an x-ray photon. (Wittke²)*

be radiated or absorbed, such as by a lattice vibration, because an electron bound to an atom has a fixed amount of energy according to the laws of quantum mechanics. When the energy is radiated back it is known as scattering. (Jenkin³)

A useful way to describe x-ray production is to consider an atom with a nucleus surrounded by electrons in energy states that correspond to different quantum numbers. The states are designated K ($n=1$), L ($n=2$), and M ($n=3$) lines; the K line being the lowest energy state, L the next lowest, and so on, as in Fig. 2. (Whittke²)

If an incident electron accelerating toward the atom has sufficient energy to eject an electron from a lower energy state, the atom will be left in an excited state. The atom can reduce its energy by emitting an electron from a higher state to produce an x-ray photon. The x-ray photon has energy equal to the difference in the electron energy levels. Therefore, an electron ejected from the K line will be filled by an electron from the L or M line to reduce the energy of the atomic system. The energy released can be referred to as K radiation. This energy will either be emitted from the atom and or eject an electron from a higher energy level. This is known as the Auger effect and the ejected electron is an Auger electron. For copper, the material used in XRD, the likelihood of K radiation escaping the atom is 41 %. Depending on which energy state the replacement electron comes from, whether L or M, the energy will manifest itself as either K_{α} or K_{β} , respectively. A material therefore may emit both K_{α} and K_{β} at the same time if more than one atom is "hit" by an electron and the holes left are being filled by different states, either L or M. The hole will most likely be filled by an electron from the L line than an electron from the M line, which is why K_{α} has greater intensity than K_{β} (Cullity⁴). From this explanation, the production of x-rays can be broken down even further by assigning

the states mentioned above their corresponding quantum numbers, that is K, L, and M are assigned the quantum number $n = 1, 2,$ and $3,$ respectively. Each n -value has a corresponding l -value, the angular quantum number, which can be $l = 0, \dots, n-1.$ The various electron states derive from the values of l such that when $l = 0,$ the state is called $s;$ when $l = 1,$ it is called $p,$ when $l = 2,$ it is called $d;$ and so on. An electron in any particular state will have a spin “up” or “down” and is assigned the value of $+\frac{1}{2}$ or $-\frac{1}{2}.$ The sum of the angular and spin quantum numbers, $j=l+s,$ distinguishes between electrons in a certain state. For example, in the case of the L state, $n = 2,$ therefore $l = 0$ or $1.$ Then for $l = 0, j = \frac{1}{2};$ for $l = 1, j = \frac{1}{2}$ or $\frac{3}{2},$ and the corresponding p-state is referred to as $p^{\frac{1}{2}}$ or $p^{\frac{3}{2}},$ respectively.

A target atom will have characteristic x-radiation depending on its electron configuration. Copper is a common target material, the type used for experimentation in this thesis, so it is useful now to consider the electron configuration of copper. The copper K spectrum consists of two α lines from $p^{\frac{3}{2}} \rightarrow 1s$ and $p^{\frac{1}{2}} \rightarrow 1s$ transitions, and are referred to as α_1 and $\alpha_2,$ respectively. In addition to $K\alpha_1$ and $K\alpha_2,$ there may also be $K\beta_1, K\beta_2,$ and $K\beta_3.$ The energy difference between the lines is simply due to its spin-orbit splitting so the relative energy difference is very small, approximately 0.78 meV. This causes only partial separation of the two wavelengths, about $0.004 \text{ \AA},$ to occur in x-ray diffraction and is usually only resolved at high angles of diffraction. The intensity ratio is equal to the number of electrons that may make the transition and can be calculated by quantum mechanics. In the case of the $K_{\alpha_1}:K_{\alpha_2}$ ratio, there are four $p^{\frac{3}{2}}$ electrons giving

rise to the $K_{\alpha 1}$ wavelength and two $p^{\frac{1}{2}}$ electrons giving rise to the $K_{\alpha 2}$ wavelength, so the expected ratio is about 2:1. Since the transition is less likely for K_{β} than for K_{α} , the ratio is actually larger. The probability for this occurrence is more complex, but amounts to approximately 5:1 in favor of K_{α} . (Jenkins³) This explanation of the difference between K_{α} and K_{β} will be useful in the discussion of filters following.

X-rays are produced in a filament tube consisting of two metal electrodes enclosed in a vacuum chamber. Electrons are produced by heating a tungsten filament cathode. The cathode is at a high negative potential and the electrons are accelerated towards the anode, which consists of a metal target, in this case copper, which is at ground potential. X-rays created in the x-ray source interact with the sample and the intensity of the resulting beam is picked up by the detector.

2.2 OPTICS

In order to produce a useful diffraction pattern, the ideal diffracted x-ray beam will consist of only one wavelength, a monochromatic beam. However, the x-ray tube must be operated above a certain excitation voltage, V_K , to ensure a useful intensity of K radiation. This is because the energy of the radiation is related to the excitation voltage by the expression,

$$eV_K = W_K \quad \text{Eq. 2.1}$$

where e is electric charge and W_K is the critical energy needed for ejection of K electrons.

Since $K_{\alpha 1}$ is the most intense wavelength, it is desirable to reduce the amount of other wavelengths, especially K_{β} since it has enough intensity to contribute to the diffraction pattern. Bremsstrahlung radiation also occurs from the electrons slowing down at different rates, emitting different amounts of energy, thus x-rays of different

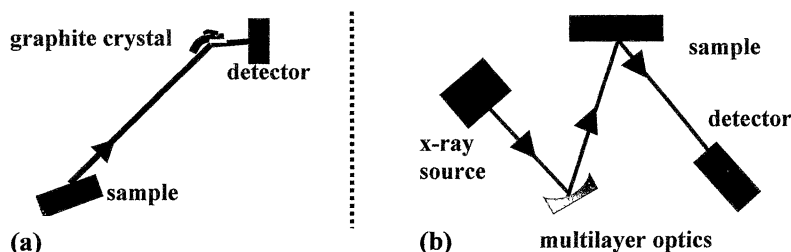


Figure 3: (a) Schematic of using graphite crystal previously to produce monochromatic x-ray beam. (b) The multilayer optics produces a more intense beam.

wavelengths. Previously a monochromating graphite crystal was placed in the diffracted beam after the sample to remove the K_{β} and other x-rays, Fig. 3. The crystal was oriented so that it diffracted only the K_{α} x-rays. However, the intensity of the K_{α} rays was significantly reduced.

Recently, advances in x-ray diffractometry have been made to allow reduction in the intensity of K_{β} rays from the detected x-ray beam while maintaining sufficiently intense K_{α} rays. The improved optical system, Fig. 4., is positioned in the path of the source to the sample and is able to collimate divergent x-rays and focus them on the sample to allow for maximum x-ray intensity. It also acts as a filter to absorb K_{β} radiation with the proper choice of mirror layer materials, such as nickel/carbon for copper radiation. In order to discuss the filtration of K_{β} , it is first necessary to discuss absorption aspects of a material. Afterward, the collimation and focusing of the beam will be discussed because these require a discussion of diffraction.

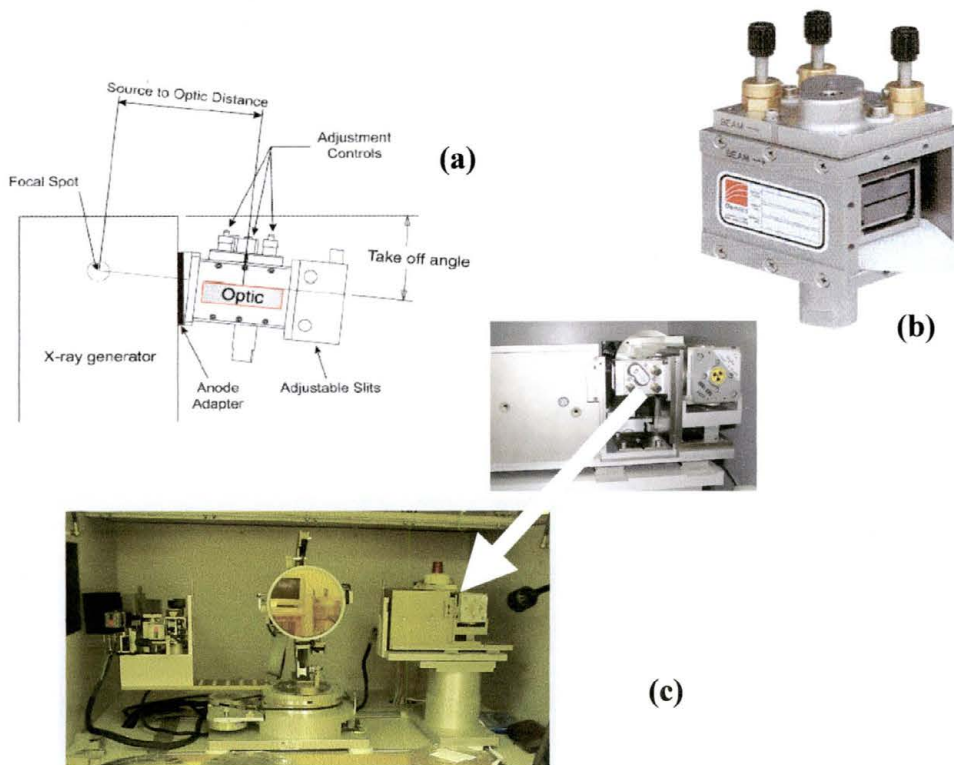


Figure 4: (a) Schematics of optics in path of incident beam, (b) actual optics, and position of optics in BEDE D1 X-Ray Diffractometer.

2.1.1 ABSORPTION

When x-rays come into contact with a material, some are transmitted and some are absorbed. The amount of x-rays absorbed depends on the linear absorption coefficient of the material, μ , related to the density of the material. The decrease in intensity is expressed by the equation,

$$-\frac{dI}{I} = \mu dx \quad \text{Eq. 2.2}$$

where I is the intensity of the incident x-ray. The integration of this expression yields,

$$I_x = I_0 e^{-\mu x} \quad \text{Eq. 2.3}$$

where I_0 is intensity of the incident x-ray beam and I_x is the intensity of the transmitted beam after passing through a material of thickness x . (Cullity⁴)

Since μ is proportional to density, ρ , the ratio μ/ρ is constant for the material and does not depend on the physical state of the material, whether it is a solid, liquid, or gas. This is known as the mass absorption coefficient and is related to the x-ray intensity by the expression,

$$I_x = I_0 e^{-(\mu/\rho)\rho x} \quad \text{Eq. 2.4}$$

so that a given material absorbs x-rays in a characteristic way. This characteristic is useful when the filtration of certain wavelengths is desired. Though the ratio μ/ρ does not depend on the state of the material, it does depend on the incident wavelength and is different for different materials depending on their atomic number, Z . It can be expressed empirically as:

$$\frac{\mu}{\rho} = KZ^4 \lambda^3 \quad \text{Eq. 2.5}$$

where K is a constant that is different on each side of the absorption edges.

To understand the concept of absorption edges, consider that an x-ray acts in a manner similar to an electron in the way it affects the electrons of an atom. As formerly discussed, an electron with enough energy can eject an electron from the K state of an atom. The same is true for an x-ray with the sufficient amount of energy, W_K (for an electron in the K state). The ejected electron is called a photoelectron and the emitted radiation is fluorescent radiation. It has the same wavelength as radiation produced by an electron ejected by another electron. The energy relates to the wavelength by the expression,

$$W_K = h\nu_K = \frac{hc}{\lambda_K} \quad \text{Eq. 2.6}$$

where ν_K and λ_K are the frequency and the wavelength, respectively, of the K absorption edge. As the equation demonstrates, the longer the wavelength, the less energy the x-ray has. The absorption edge refers to the critical energy W_K for ejection of an electron from the K state, depending on the binding energy of the electron. From this relationship, it is apparent that as energy of the x-ray decreases, the wavelength increases as does likelihood of it being absorbed. At a particular wavelength, the absorption of the K state of an atom no longer contributes to the total absorption, therefore the total absorption immediately decreases and then begins to increase again with wavelength until the different states of the L state are no longer able to contribute and so on. This means a dramatic decrease in intensity occurs, since intensity relates to the mass absorption coefficient exponentially (Jenkins³)

2.1.2 FILTRATION

This decrease in intensity is useful when obtaining diffraction patterns if the K_β intensity is reduced relative to the K_α intensity. This is done by introducing a material that acts as a filter. The filter has an atomic number of one less than the target metal. For a copper target, a nickel filter is chosen because the absorption edge lies directly between the wavelengths of K_α and K_β , see Fig. 5. The K_β ray has enough energy, or short enough wavelength, to eject an electron from the K state of the atom, while the K_α ray does not and passes through. This is simply due to the phenomenon discussed earlier, mainly that it takes more energy to produce a K_β ray than a K_α . It follows from the conservation of energy that the resultant K_β ray has more energy than a K_α .

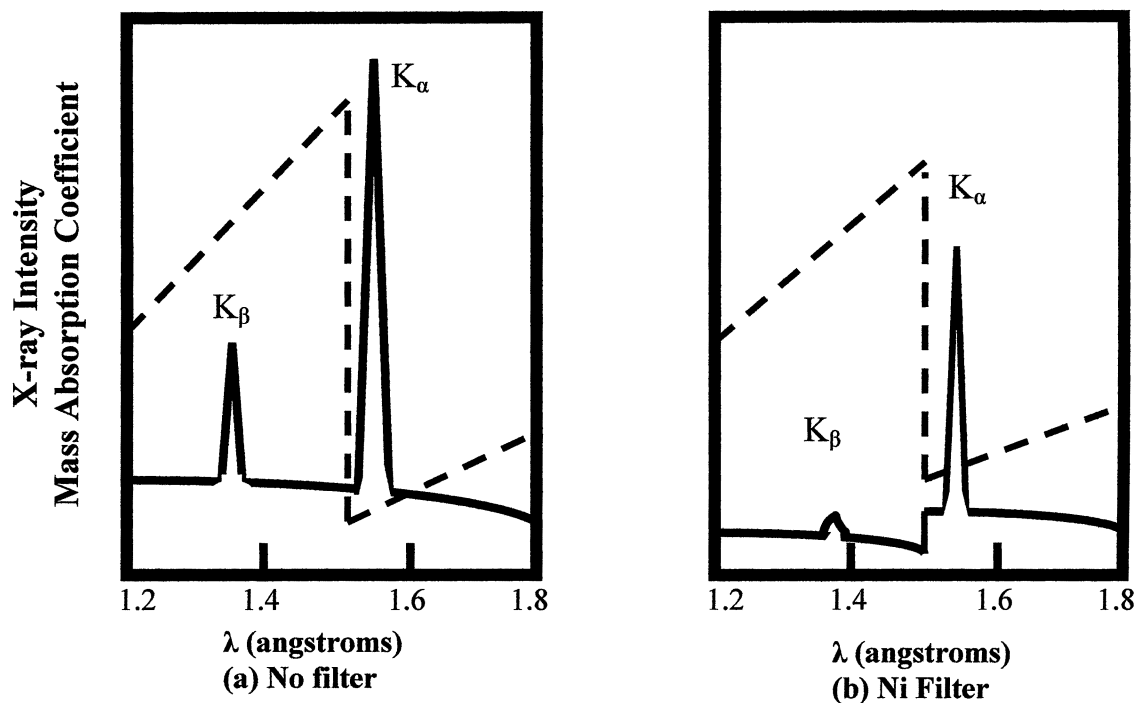


Figure 5: Comparison of the spectra of Cu radiation (a) before and (b) after passage through a nickel filter. The dashed line is the mass absorption coefficient of Ni. (Cullity⁴)

2.1.3 CRYSTAL DIFFRACTION

If a beam of light falls on a screen perforated with holes arranged in a regular pattern whose spacings are comparable with the wavelength of light, diffraction occurs. The light consists of a weakened beam in the direction of the incident light, but also of other, regularly arranged separate beams, deviated by specific angles which depend on the ratio of the wavelength of light to the spacings of the pattern. The diffraction is due to the interaction of the repeating pattern with the repeating light waves. A crystal is a solid that consists of atoms arranged in a repeating three-dimensional pattern. An x-ray that encounters the atomic plane of a crystal will behave much like the light wave mentioned above. This is demonstrated using the principle of Bragg's Law,

changing the path lengths, a crystal can be identified according to its d-spacing. That is, where diffraction occurs there will be an intense peak of intensity in the diffraction pattern at that particular angle. (Jenkins³)

A crystal is not made up of simple parallel planes of atoms, however. Instead, it consists of repeating unit cells, within which are found a set of parallel planes, as seen in Fig 7. These planes may have different orientation from one cell to the next and therefore the crystal must be rotated to allow all reflections to be observed. (Lattman⁵)

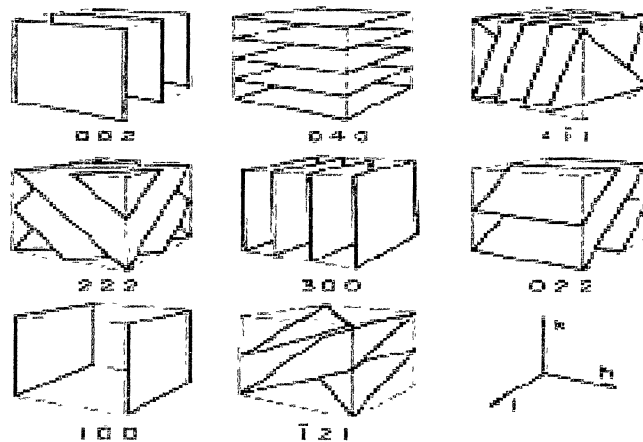


Figure 7: Unit cells consists of a set of parallel planes which have different orientations depending on the structure of the unit cell (Lattman⁵).

2.1.4 COLLIMATE AND FOCUS

The multilayer optics are arranged so that d , now the spacing of the multilayer, is equal to the sum of the thickness of one layer pair of materials consisting of high-Z and low-Z materials, as in Fig. 8. Alternating layers of high-Z and low-Z materials create a periodic structure of differing electron densities, like the atomic planes in crystals.

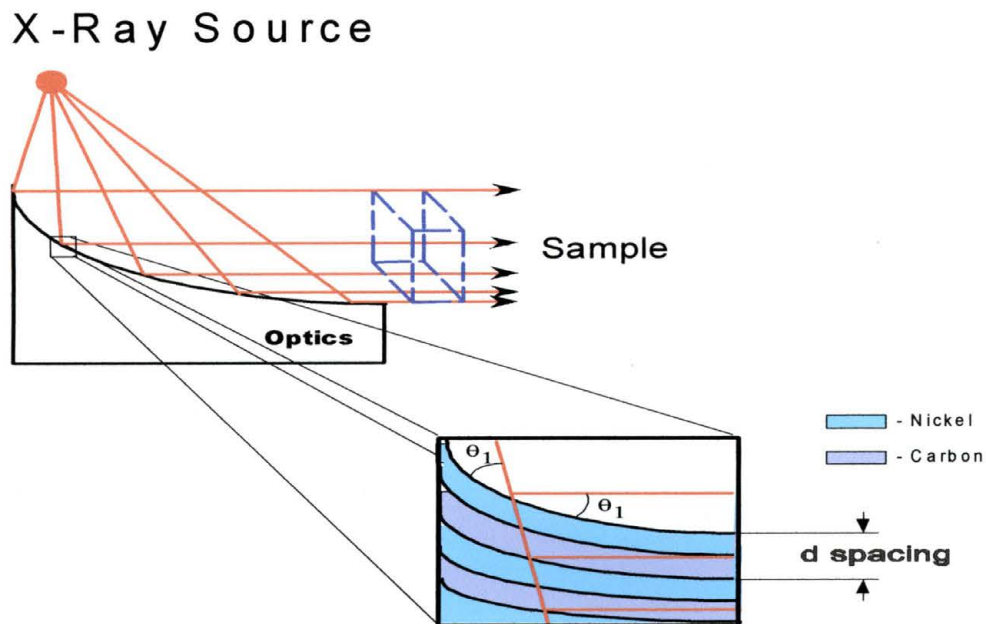


Figure 8: Schematic of nickel-carbon interface at surface of mirror

The materials chosen for copper radiation are carbon, as a low-Z material, and nickel as a high-Z material which as explained previously doubles as a filter. The density of the nickel is high enough to allow x-ray diffraction off the surface. The carbon layer is less dense and x-rays are allowed to pass through before they hit another nickel surface where more are diffracted. The nickel layer also acts as a filter of K_{β} rays as mentioned before. The shape of the mirror is parabolic so that x-rays with different incident angles will be diffracted in a parallel beam, as seen below. If the phases of the waves scattered from each layer coincide, the multilayer will achieve maximum reflectivity. A parabola will reflect radiation emitted from its focus in a parallel beam, see Fig. 9. The incidence angle on the parabola of a ray emerging from the focus **F** depends on the point of incidence **A**. For a parabola defined by the equation:

$$y^2 = 2px, \quad \text{Eq. 2.8}$$

where p is the parabola parameter, the incidence angle of the focal ray FA is:

$$\Theta_p(f) = \arccot \left(\frac{2f}{p} - 1 \right)^{\frac{1}{2}}, \quad \text{Eq. 2.9}$$

where f is the focal length, the distance between F and A . (Schuster⁶)

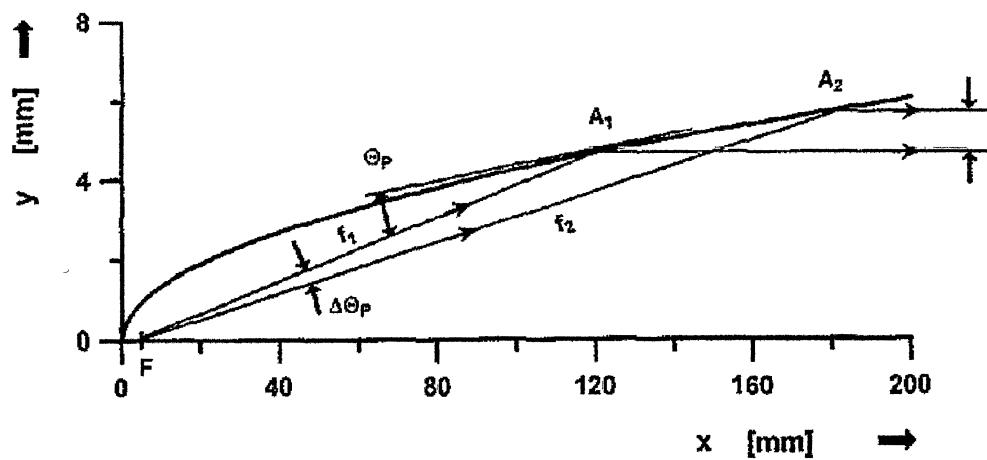


Figure 9: A ray bundle reflected on a parabola. F is the focus, A_1 and A_2 are the incidence points, and f_1 and f_2 are focal lengths. Θ_p is the incidence/reflection angle. $\Delta\Theta_p$ is the opening and Δy is the width of the parallel ray bundle. (Schuster⁶)

2.2 NANOPOWDER PARTICLE SIZE AND STRAIN DETERMINATION THEORY

As discussed earlier, diffraction will only occur when the Bragg Law is satisfied. This is useful for thick crystalline samples. However, at small particle sizes, the laws of diffraction become more complex. For instance, particles less than one micron thick tend to lack the depth necessary to cancel scattering from a plane with a non-integer λ -coefficient. Therefore, the diffraction peak begins to show intensity at θ -values lower than the Bragg angle, as well as end at θ -values higher than the Bragg angle. This is known as peak broadening and can give clues to characteristics of the particle such as grain size and crystal strain.

Particle size can be determined from the full-width-half-max (FWHM) of a diffraction peak whose maximum intensity is at θ_B , the Bragg angle using Scherrer's formula. If the atomic plane considered is designated m , it can be said using Bragg's Law that,

$$\begin{aligned} (m+1)\lambda &= 2d \sin \theta_1 \\ (m-1)\lambda &= 2d \sin \theta_2 \end{aligned} \quad \text{Eq. 2.10}$$

where $m+1$ and $m-1$ are the planes above and below the m^{th} plane, respectively, and θ_1 and θ_2 are the end values of the diffraction peak, lower and higher than θ_B , respectively. Solving for d yields an estimation of the particle size.

We begin by subtracting the two equations,

$$2d(\sin \theta_1 - \sin \theta_2) = \lambda \quad \text{Eq. 2.11}$$

$$2d \cos\left(\frac{\theta_1 + \theta_2}{2}\right) \sin\left(\frac{\theta_1 - \theta_2}{2}\right) = \lambda; \quad \text{Eq. 2.12}$$

Since θ_1 and θ_2 are approximately equal to θ_B , it is possible to assume,

$$\theta_1 + \theta_2 = 2\theta_B, \quad \text{Eq. 2.13}$$

and using the approximation that for small θ that $\sin\theta = \theta$,

$$\sin\left(\frac{\theta_1 - \theta_2}{2}\right) = \left(\frac{\theta_1 - \theta_2}{2}\right). \quad \text{Eq. 2.14}$$

Solving for d yields,

$$2d\left(\frac{\theta_1 - \theta_2}{2}\right)\cos\theta_B = \lambda \quad \text{Eq. 2.15}$$

and multiplying λ by the Scherrer constant, K , gives,

$$d = \frac{K\lambda}{B\cos\theta_B} \quad \text{Eq. 2.16}$$

This result is known as Scherrer's formula, where K is usually assumed to be 0.9.

(Cullity⁴)

In addition to the broadening caused by the particle, there exists broadening caused by strain. If the stress is uniform within the crystal, there will be a shift in the location of the diffraction peaks. This is known as macrostress. There is also a condition called microstress which is caused by dislocations, vacancies, defects, thermal expansions and contractions, etc. This will alter the d-spacing of the crystal by bending the atomic planes in a wedge shape. The result is that, overall, the average d-spacing is the same, but the d-spacing at the bottom of the wedge is lower than the overall average and vice versa for the top of the wedge. Thus, the location of the diffraction peak is the same, the θ_B does not change, but there is a broadening of the diffraction peak. In order to determine the relationship of the broadening to the angle, it is necessary to differentiate over Bragg's Law:

$$d = \frac{2\sin\theta}{\lambda} \Rightarrow \frac{\Delta d}{\Delta 2\theta} = -\frac{2\cos\theta}{2\lambda} \Rightarrow \Delta 2\theta = -\frac{\Delta d\lambda}{\cos\theta} \quad \text{Eq. 2.17}$$

Next we substitute λ back into the equation,

$$\lambda = \frac{2 \sin \theta}{d} \Rightarrow$$

$$\Delta 2\theta = -\frac{\Delta d}{\cos \theta} * \frac{2 \sin \theta}{d} = -2 \frac{\Delta d}{d} \tan \theta \quad \text{Eq. 2.18}$$

The broadening due to strain is equal to $\Delta 2\theta$ where a fractional variation in Bragg plane spacing, $\frac{\Delta d}{d}$, is the result of the variation in strain. This value includes both the tensile and compressive strength and, if the two are assumed to be equal, can be divided by two to obtain values for each.

The total peak broadening is the sum of the broadening due to size and that due to strain. Values for size and strain can be determined from the experimental broadening by subtracting out any instrumental broadening and constructing a plot of the function,

$$B_{total} = B_{exp} - B_{inst} = \frac{K\lambda}{d \cos \theta_B} + \left(-2 \frac{\Delta d}{d} \right) \tan \theta_B$$

$$\frac{B_{total} \cos \theta_B}{\lambda} = \left(-2 \frac{\Delta d}{d} \right) \sin \theta_B + \frac{K}{d} \quad \text{Eq. 2.20}$$

where the slope of a linear fit is equal to the strain and the size is given by the Scherrer constant, K , divide by the y-intercept.

These calculations are necessary for determining details about size and strain of a material. However, the crystal structure of the material and its elemental composition can be determined from comparing the location and intensities of the diffraction peaks to expected values. This type of observation was done for the cobalt silicides to be discussed in the next section.

2.3 COBALT SILICIDES FOR ULTRA LARGE SCALE INTEGRATION

Silicide thin films are an important aspect of integrated circuit technology. In logic chips, silicides are often used on source/drain junctions as well as gates and local interconnects. In order to create fast circuit performance and large device drive current, low resistance metal must be used in forming contacts to the gate and source and drain. (Gambino⁷) Thus, silicide film materials are interesting to investigate from a technological as well as fundamental point of view.

Currently TiSi_2 is most widely used because it has low resistivity and high thermal stability. It also reduces native oxides in contacts because of the high affinity of titanium to oxygen. Titanium produces a very stable and thin, 1 Å, tetragonal titanium dioxide layer with protective characteristics (Popp⁸). However, industry has already begun the transition to replacing TiSi_2 with CoSi_2 . CoSi_2 is an alternative to TiSi_2 because, though its resistivity and thermal stability are similar to TiSi_2 , the sheet resistance of CoSi_2 is relatively insensitive to decreasing linewidth compared to TiSi_2 , which shows an increase in sheet resistance when grown on polysilicon on linewidths narrower than 0.25 μm. This is because TiSi_2 forms in two phases, C52-polymorph and C49-polymorph. At 0.25 μm, gate heights and contact junction depths are in the 200 nm range, thus the TiSi_2 thickness is typically on the order of 50 nm. At this depth, the C54 phase has a resistivity of 15-20 μΩ-cm. For narrower lines, the C49 phase is dominant, since C54 is formed due to a nucleation-limited process in the C49 phase and the smaller lines contain less nucleation sites. The problem that arises is that the resistivity of the C49 phase is 4-5 times that of the C54 leading to a drastic increase in resistance.

However, CoSi_2 forms in only one phase and has a resistance similar to C54 phase TiSi_2 . CoSi_2 also has less agglomeration and bridging than TiSi_2 for MOS line widths less than $0.13\ \mu\text{m}$ as well as high thermal and chemical stability. Also, its electrical properties are independent of Si doping and it can be manufactured with acceptable adaptations to standard MOS process manufacturing.

This makes it an attractive alternative to TiSi_2 , though there are some drawbacks, such as the interface oxygen layer that grows between the CoSi_2 and the silicon substrate during formation of the silicide layer. This is caused by oxygen contamination from the ambient or the wafer itself. This creates non-uniform thickness, may impede or prevent silicidation, and can cause increased junction leakage (Roy⁹). One idea is to sputter a thin layer of titanium on top of the cobalt. The theory is that the titanium cap protects the cobalt silicide from ambient oxygen and acts as a getter for oxygen at the cobalt-silicon interface. This enables the CoSi_2 to form more quickly and with greater uniformity (Detavernier¹⁰). X-ray analysis can be used to compare silicide formation between titanium-capped cobalt and cobalt without a titanium layer.

CHAPTER 3

DATA & ANALYSIS

3.1 POWDER X-RAY DIFFRACTION PATTERNS

In order to test the peak broadening theory mentioned in Chapter 2, several different sizes of MgO were tested using high-angle x-ray diffraction (HAXRD) measurements. The powders were ordered from Nanostructured & Amorphous Materials, Inc., Los Alamos, New Mexico, and NanoScale Materials, Inc., Manhattan, Kansas. The resulting diffraction patterns can be seen in Fig. 10. for MgO.

Sample	Manufacturer	Particle Size (nm)	Crystallite Size (nm)
1	NanoScale Materials, Inc.	3000*	<8
2	Nanostructured & Amorphous Materials, Inc.	36	8
3	Nanostructured & Amorphous Materials, Inc.	100	8

Table 1: Average particle and crystallite size of MgO nanopowder as given by manufacturer. Particles consist of individual crystallites.

*NanoScale reports the agglomerate size of its MgO particles.

The average particle sizes for two of the samples were given as 36 nm and 100 nm by the manufacturer, Nanostructured & Amorphous Materials, Inc.; the NanoScale sample specifies that the NanoActiveTM material agglomerate size is 3 μm , see Table 1. Agglomeration is caused by static and other weak forces acting on the small particles and poses a serious problem in that it has a negative affect on function of the nanopowder¹¹. The actual particle size of sample one appears from simple observation to be smaller than

samples two and three. The dispersed particles can be seen with TEM analysis to confirm this observation in Fig. 15. As expected, the peak broadening increases from the 100 nm particle size sample to the 36 nm particle size sample and is greater still for the NanoActive™ sample. It is also important to note that intensity decreases with particle size along with the number of discernable peaks, making diffraction analysis difficult, especially since more than two peaks are needed for useful calculations. Table 2 shows the 2Theta-Omega angle and FWHM values used to calculate size and strain for each sample with a Williamson-Hall plot.

Sample	2Theta-Omega(deg)	FWHM(deg)
1	42.03480	3.3687
	61.35115	3.9489
2	42.68908	0.5986
	62.18523	0.7053
	78.55368	0.9157
3	36.75678	0.5754
	42.86683	0.4022
	62.36013	0.4372
	74.79035	0.6762
	78.69530	0.5559
	94.60588	0.7967
	109.9672	0.7976

Table 2: *Diffraction peak values used for Williamson-Hall plot.*

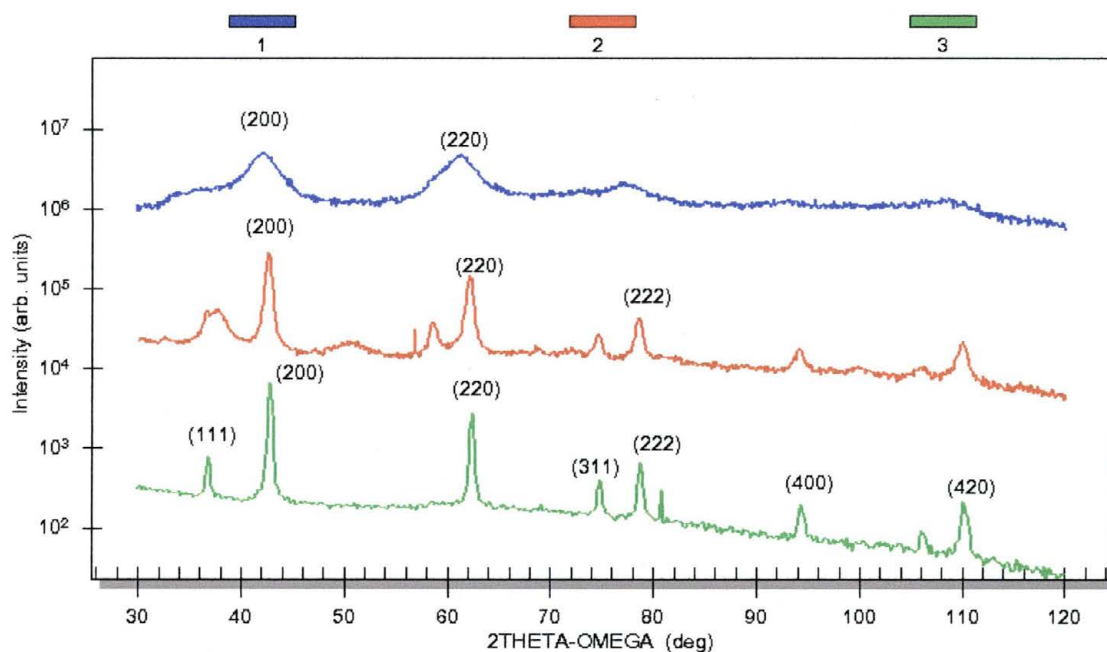


Figure 10: Comparison of XRD data for three different grain sizes of MgO. (Sample numbers correspond to sizes given in Table 1.) Additional peaks seen for the smaller sizes may actually be due to that size's affinity for reacting with water in the atmosphere.

3.1.1 LaB₆ STANDARD CALIBRATION

This can be tested using the Scherrer equation discussed above. However, first a correction must be made to subtract the line broadening caused by the instrument itself. In order to do this, a standard is chosen with a very large grain size, that is, $> 1000 \text{ \AA}$, which will not produce peak broadening (Cullity⁴). The standard must also have no strain, meaning it is very brittle and essentially will break before it bends. The large grain size and lack of strain will not broaden the peaks, therefore all broadening is assumed only instrumental.

Lanthanum Hexaboride powder from National Institute of Standards and Technology (NIST), LaB₆ Standard Reference Material (SRM) 660a, was chosen as the instrumental standard. The size of the particles as given by NIST ranges from 2 to 5 μm and show no signs of strain. The powder was prepared by spraying a glass slide with ordinary hairspray and allowing a thin layer of powder to dry on the surface. A HAXRD

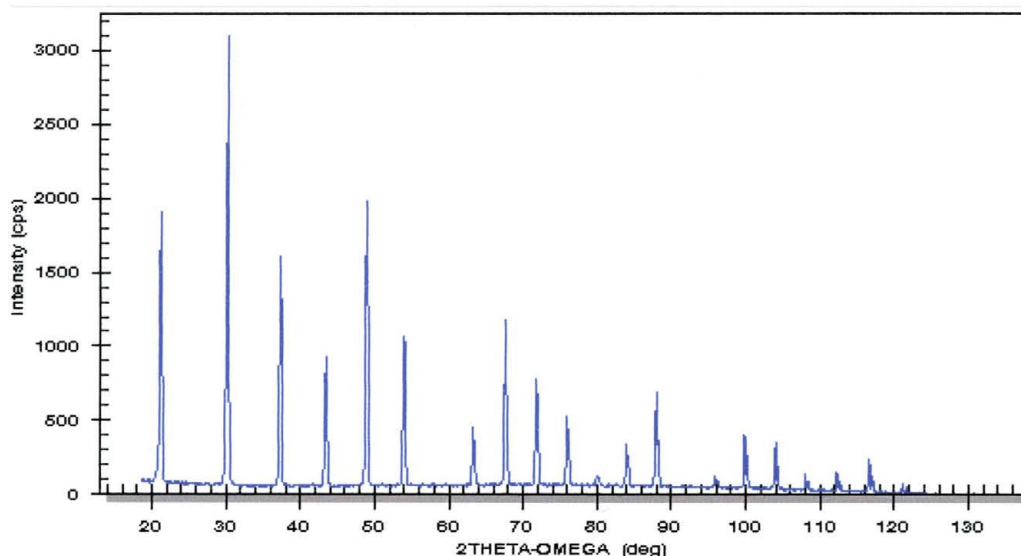


Figure 11: *HAXRD of LaB₆ Standard Reference Material; peak broadening is due only to instrumentation*

measurement with a step size of 0.1 can be seen in Fig. 11.

The full-width at half-maximum (FWHM) for each peak was then plotted against its corresponding 2Theta value in order to obtain a least fit polynomial curve. The equation of the curve fit was used to find instrumental broadening, B_i , for other samples at the 2Theta value for a given peak. This broadening could be subtracted from the observed broadening, B_o , to find the resultant broadening caused by size and strain, B_r .

The resulting plot with the curve fit can be seen in Fig. 12.

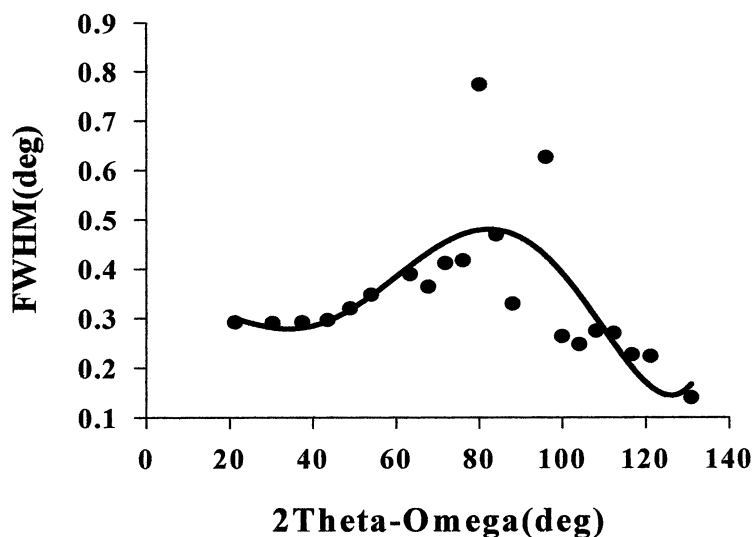


Figure 12: Least fit polynomial curve of FWHM vs. 2Theta-Omega for LaB6 standard.

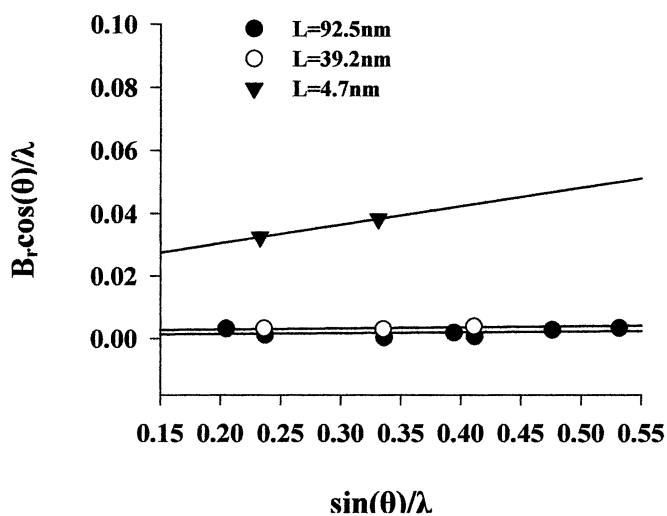


Figure 13: Williamson-Hall plot for size and strain determination for varying MgO sample sizes. The calculated values of 92.5, 39.2, and 4.7 nm correspond to manufacturer sizes of 100 nm, 36 nm, and NanoActive™ respectively. The strain for the NanoActive™ material is greater than that of the other two made by Nanostructured & Amorphous Materials, Inc and it is unclear whether this is a function of the size difference or the manufacturing process, for which neither company would give information.

3.1.2 PARTICLE SIZE AND STRAIN DETERMINATION FOR MgO NANOPOWDER

The particle size and strain value for each MgO sample was then calculated by plotting $B_r \cos \theta$ as a function of $\sin \theta$, known as a Williamson-Hall plot shown in Fig. 13. This type of plot assumes the peaks to be Lorentzian. (Cullity⁴) The linear curve fit equation from this plot was used to calculate the particle size and strain. The sizes were calculate by dividing the Scherrer constant, $k = 0.9$, by the y-intercept of the line. Strain is determined by the slope of the line. The sizes of 92.5 nm and 39.2 nm correlate to the manufacturer given sizes of 100 nm and 36 nm, respectively. The 4.7 nm size is for the NanoActiveTM material and qualitatively agrees with the TEM measurements shown in the following section. The strain for the NanoActiveTM material is greater than that of the other two made by Nanostructured & Amorphous Materials, Inc and it is unclear whether this is a function of the size difference or the manufacturing process, for which neither company would give information. The difference may be because only two useful peaks were achieved for sample one, which is one of the shortcomings of Williamson-Hall plot calculations

Another method of calculating size is a program developed by Dennis Eberl, et. al., of US Geological Survey, Boulder, Colorado. The program is in the form of an excel spreadsheet called MudMaster. It uses the peak intensities to determine the interference function which can then be composed into a Fourier series. The theory and procedure for using the program can be found at the website¹². A comparison of size determined by the Scherrer equation, Eq. 2.16, Williamson-Hall Plot, and MudMaster can be found in Table 2. There is less than two nanometers difference between the crystallite size given by the

manufacturer for samples two and three and the MudMaster calculation. It may be coincidence that the sizes found by Scherrer and Williamson-Hall are similar to the particle size, as x-ray diffraction analysis gives information about crystallite size, not particle size. Gas absorption analysis was done by Dennis Eberl and his colleague David Rutherford to test particle size for sample two and revealed a diameter of 38nm.

SAMPLE	METHOD	SIZE (nm)
1	Scherrer	2.8
	Williamson-Hall	4.7
	MudMaster	2.7
2	Scherrer	27.6
	Williamson-Hall	39.2
	MudMaster	9.5
3	Scherrer	78.4
	Williamson-Hall	92.5
	MudMaster	9.8

Table 3: Comparison of three methods of size determination; Scherrer, Eq. 2.16, Williamson-Hall Plot, Fig. 13, and MudMaster.

3.1.3 TEM

The size of the particles was also measured using a JEOL 1200 EXII transmission electron microscopy (TEM). TEM analysis generates an image of the sample based on electron scattering. Electron scattering is very sensitive to the target element and atoms

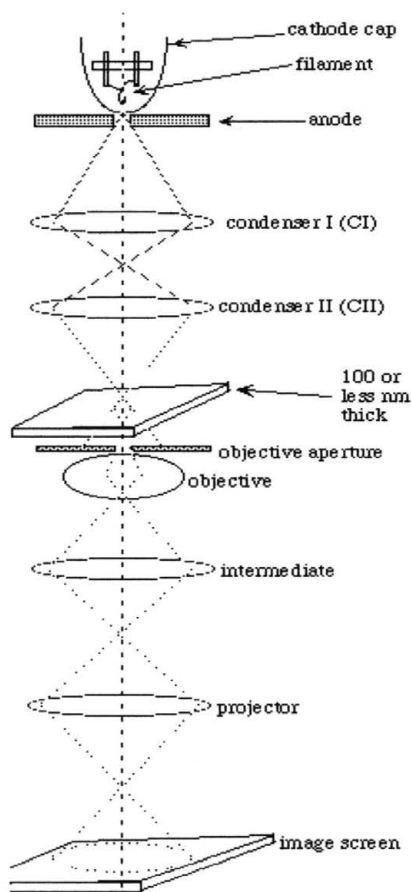


Figure 14: *Schematic of transmission electron microscope, TEM. Electrons are produced by the electron gun and focused onto the sample by two condenser lenses. The interaction of the electrons as they pass through the sample form an image. Areas of the sample that are very electron dense will appear darker than areas which are not and allow electrons to pass through with little or no interaction. (Koke¹³)*

with a high atomic number will scatter electrons more effectively than those with a lower number. Elastic scattering in which the electron does not lose energy occurs when the electron is scattered by the nucleus of the atom. An electron scattered by the electron cloud of an atom loses energy and this is known as inelastic scattering. The type of scattering that occurs determines the contrast of the image and atoms with a high atomic number appear darker than those with a lower atomic number (Sickafus¹⁴). A diagram of the electron optics of the TEM can be seen in Fig. 14. The electron gun produces a

stream of electrons. The electrons are focused into a beam by the first condenser which controls the spot size of the beam. The second condenser focuses the beam onto the sample and controls the brightness of the image; the image is brightest when the focus is on the sample, dimmer when the focus is above or below the sample. The sample is mounted on a copper grid and placed into the beam path. The sample must be very thin, on the order of 100 nm or less, so that the electrons can transmit through the less dense areas of the sample.

The objective aperture enhances contrast by blocking out electrons that deviate from the optical axis. The transmitted electrons are then focused by the objective lens onto the image screen. The intermediate lens controls magnification while the projector screen controls the dimensions of the image on the screen. The luminescent image screen causes light emission when hit by electrons. Thus, dense areas of the sample where less electrons are able to transmit through appear darker.

The traditional way to view nanopowders with the TEM is to sonicate the sample in de-ionized water and place this solution on a carbon or Formvar®-coated grid. The Formvar® grids along with an embedding method were both attempted and compared to see which gave the best image. The embedding method was performed by depositing a small amount of powder into the tip of an embedding capsule and mix with a small amount of Spurr epoxy resin (SER). The resin acted as a suspension for the particles to be sliced into thin sections after hardening. Most sections would wrinkle up and be too thick for use, so the more conventional method was used.

The conventional method of analyzing nanopowders with TEM consists of a thin plastic film covering the copper grid. The grids can be covered by dropping a solution

0.25% or 0.5% polyvinyl formal (Formvar®) in ethylene dichloride or chloroform onto a water surface. The solution floats on the water and the grids can then be placed on the solution and scooped out with paper. The nanopowder is sonicated for twenty minutes in deionized water and small droplets of the solution are placed on the grids with a syringe and allowed to dry. This method produced the best results, which can be seen in Fig. 15.

The smallest particles are in agreement with the size given by the manufacturer as well as the size calculated from x-ray diffraction. The larger particles may actually be clumps of smaller particles. The striations in the image are due to converting the negative images into digital format (.jpg) and not artifacts of the original images.

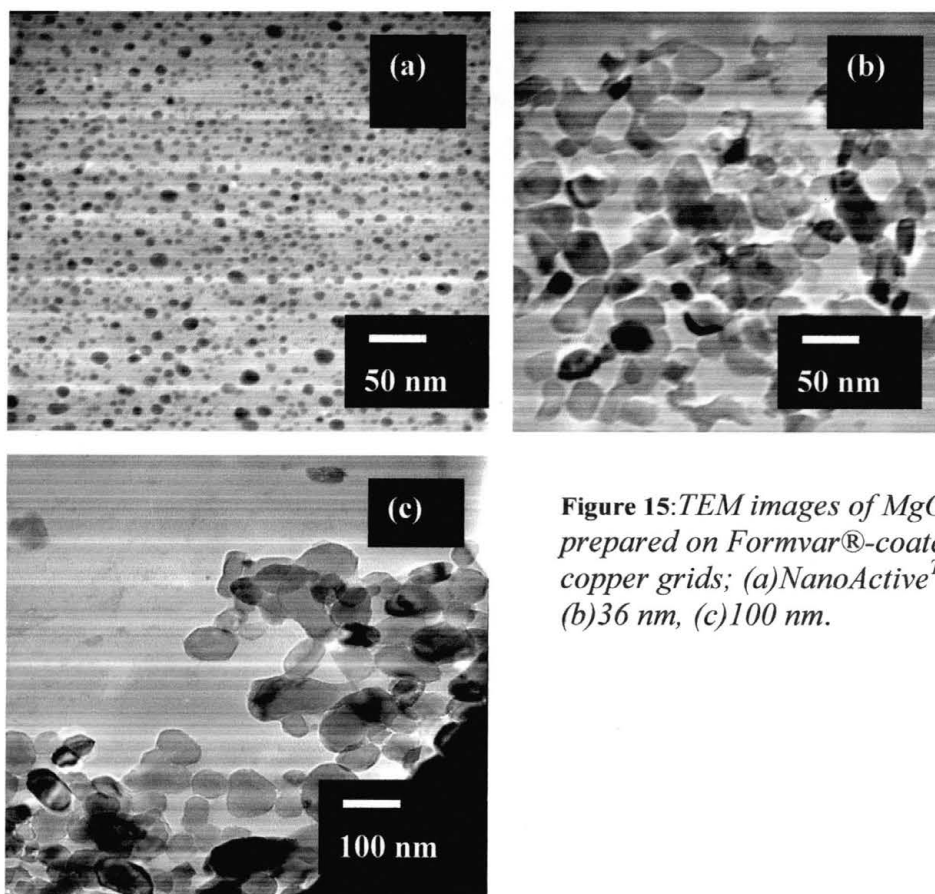


Figure 15: TEM images of MgO prepared on Formvar®-coated copper grids; (a) NanoActive™, (b) 36 nm, (c) 100 nm.

3.2 COSI₂ DIFFRACTION PATTERNS

Cobalt silicide films were created by Agere Systems for structural and magnetic characterization. The films were formed from the rapid thermal annealing (RTA) of magnetron sputtered cobalt films on silicon typical for the silicide process used in modern integrated circuit device fabrication. The silicon substrate was first cleaned with a solution of 0.5 % hydrofluoric acid in water. The cobalt film was then magnetron sputtered at 200 °C at a pressure less than 5 mtorr. The first anneal (RTA1) was done at 550 °C for thirty seconds and then a cobalt strip was performed with a solution of 5 % ammonia hydroxide and 20 % hydrogen peroxide in water (APM). APM is also known as SC1 (RCA Standard Clean #1). This was done in combination with a cleaning solution of 25 % sulfuric acid in hydrogen peroxide (SPM). The second anneal (RTA2) was done at 825 °C, again for thirty seconds.

Three sets of wafers were analyzed using x-ray diffraction. One set consisted of four wafers, initially with a 100 Å layer of cobalt, at each stage of fabrication; before RTA1, after RTA1, after stripping, and finally after RTA2. A second set consisted of three wafers; also with a 100 Å layer of cobalt and an additional 90 Å layer of Ti; after RTA1, after stripping, and after RTA2. A final set included three wafers, initially with a 400 Å layer of cobalt, at each stage of fabrication; before RTA1, after RTA1, and after RTA2.

3.2.1 ATOMIC FORCE MICROSCOPY FOR SURFACE ROUGHNESS ANALYSIS

Each wafer, except the initial Co layer, also underwent atomic force microscopy testing at Agere Systems to evaluate surface roughness, Chart1 and Fig.16. As can be seen clearly from the AFM data, the strip performed on the film after the first anneal

decreases the roughness by one or two angstroms, while the second anneal increases the roughness by about a factor of three or four.

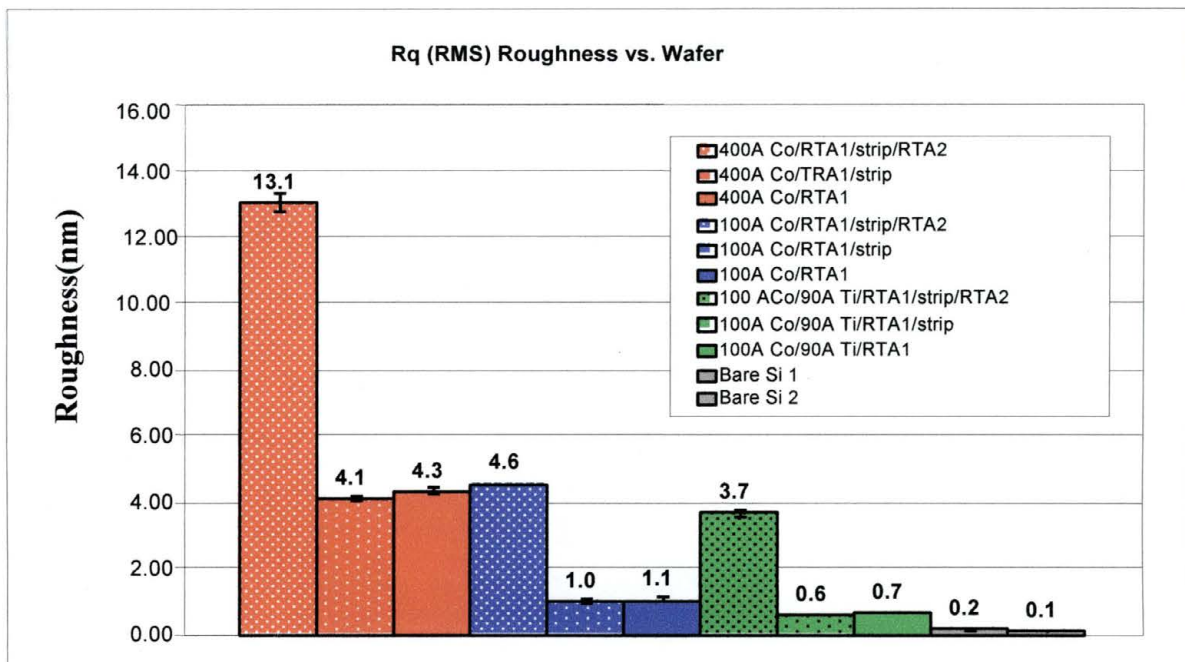


Chart 1: Average roughness data for all Co silicide films, including bare Si. The error bars result from the standard deviation in the roughnesses measured for the same sample.

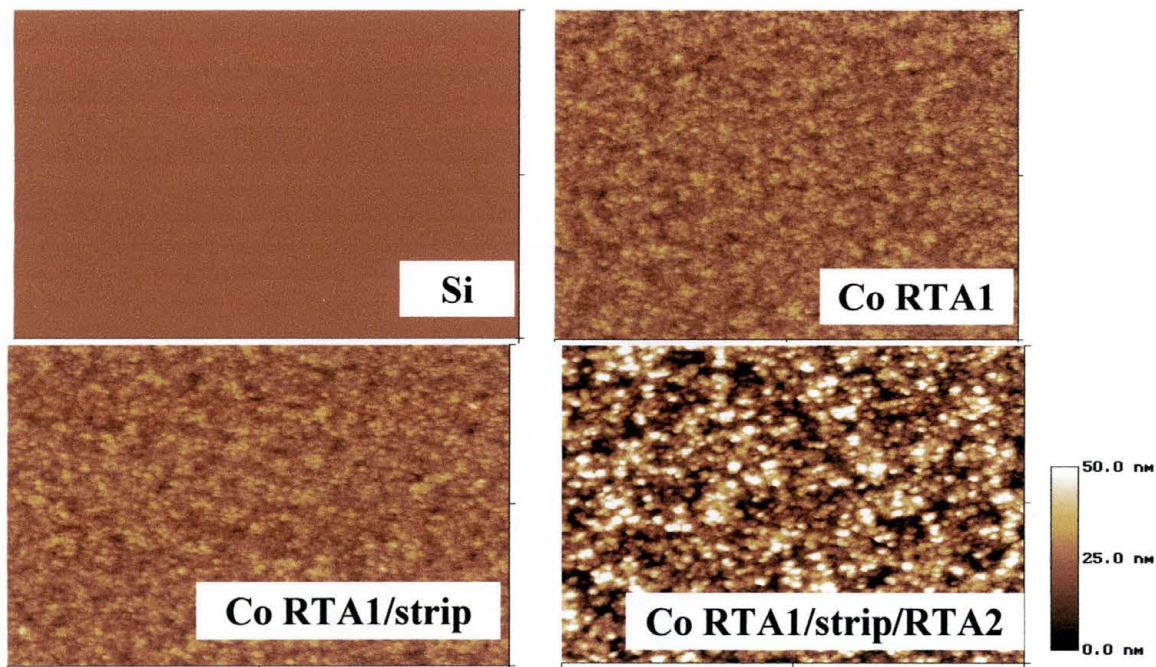


Figure 16: AFM data for 400 Å wafers, including bare Si reference

3.2.2 PBXRD, HAXRD, AND XRR

Three different x-ray characterization tests were performed on each wafer. These include, glancing incidence parallel beam powder diffraction (PBXRD), high angle x-ray powder diffraction (HAXRD), and x-ray reflectivity (XRR). Each type of measurement reveals different characteristics of the film so that much can be learned about the film by looking at all three measurements. Extensive discussion including the theory and operation of the x-ray diffractometer can be found in previous theses (Tijerina¹⁵, Ayala¹⁶).

PBXRD scans are taken at a very low angle of incidence, thus allowing the beam to travel through more of the film at an angle nearly parallel to the surface of the film. Fig. 17. shows PBXRD scans of each wafer, separated according to the film thickness as given by Agere. The indices of the planes are determined using data from the International Center for Crystal Diffraction Data (ICCD), which identifies at what value of 2θ a diffraction peak should be observed, the relative intensity of that peak to other peaks in the scan, and the indices of the plane at that angle. At peaks with a relatively high intensity, it is possible to deduce that the crystal orientation is very random, in that there are a great number of planes for the beam to go through. This is most evident in the 400 Å film where the same peaks are shown with a greater intensity than the thinner films. The peaks correspond to those expected according to the ICCD for CoSi after the first RTA as well as CoSi₂ after the second.

A good way to confirm conclusions obtained from PBXRD is to do the same scan at a high angle, HAXRD. This scan is taken with the incident beam at an angle to the film equal to that between the film and the detector. Fig. 18. shows HAXRD scans of the same films. For films whose crystal orientation is parallel to the surface, the intensity will be high at specific values of 2θ . The as-deposited cobalt (111) peak is seen in the high angle scans, but not the parallel beam scans. This leads to the conclusion that the crystal orientation of the as-deposited film is parallel to the surface. The (111) peak in the cobalt film before annealing indicates an initial fcc structure. The reason for this is unclear, as literature shows cobalt sputtered at this temperature (200 °C) to have an hcp structure. (Ivanova¹⁷)

However, after annealing, the parallel beam scans exhibit increased intensity compared to the high angle scans, by a factor of about four. This suggests that during annealing, amorphous silicide layers are formed. The conclusion that the film becomes increasingly rough at the interface can be supported by the last type of x-ray measurement.

XRR scans can be used to determine many more properties of the film and even layers forming between the surface layer and the substrate. For this type of scan, the beam is incident at the critical angle causing reflectivity and creating interference patterns. Reflectivity scans do not depend on diffraction laws (Bragg mentioned previously), but instead rely on the index of refraction of the material which is based on its electron density. From this pattern, properties of the film layers such as composition, density, thickness, and roughness can be determined by fitting the data to a computer model. Fig. 19. shows XRR scans of each film.

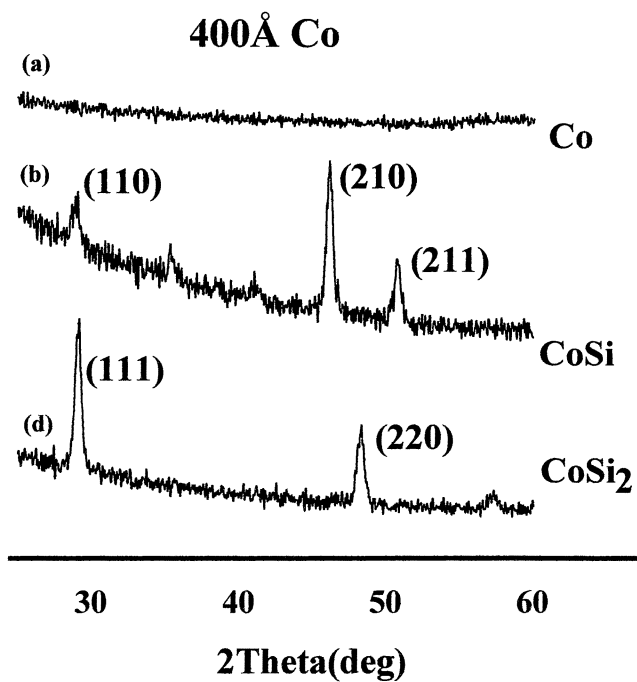
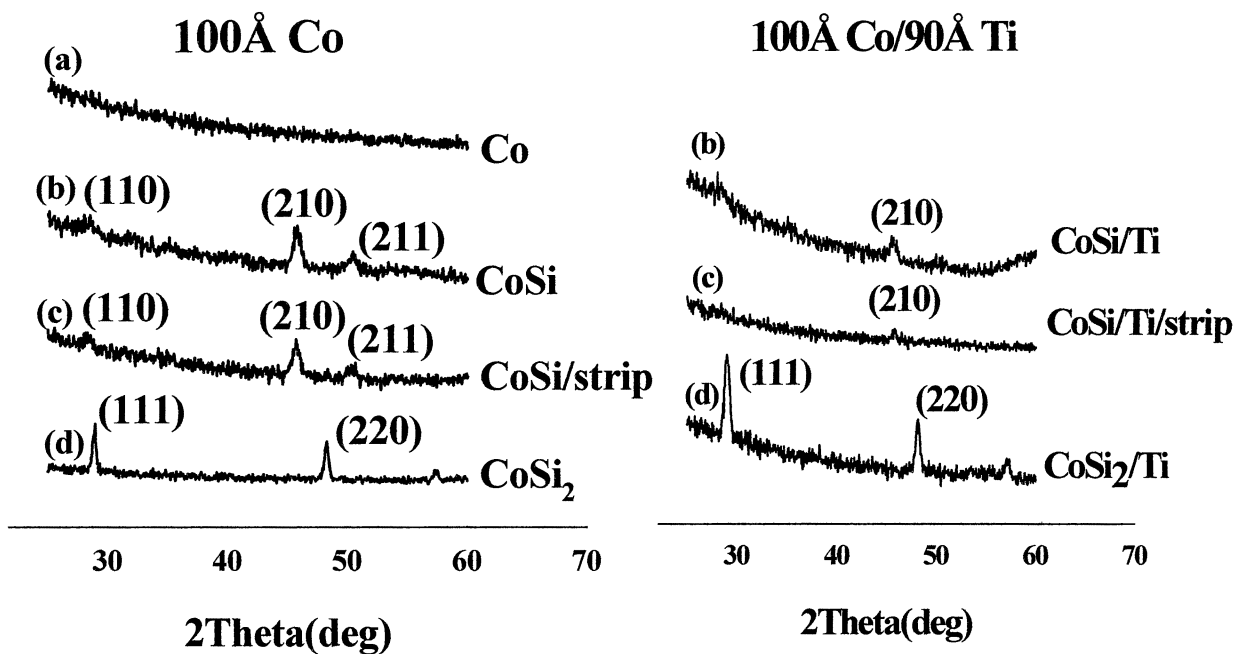


Figure 17: PBXRD scans for (a) as-deposited cobalt, (b) RTA1, (c) RTA1/strip, (d) RTA1/strip/RTA2. The scans reveal a more textured film after annealing than the as-deposited cobalt film, as well as the formation of CoSi and CoSi₂ after the first and second anneal, respectively.

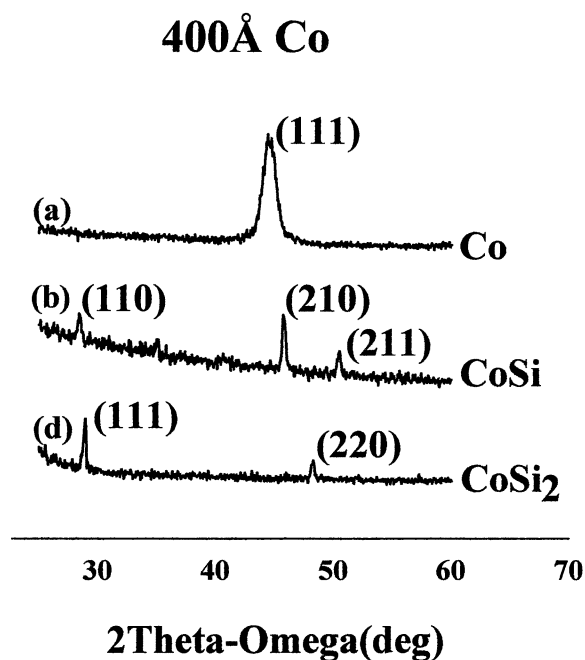
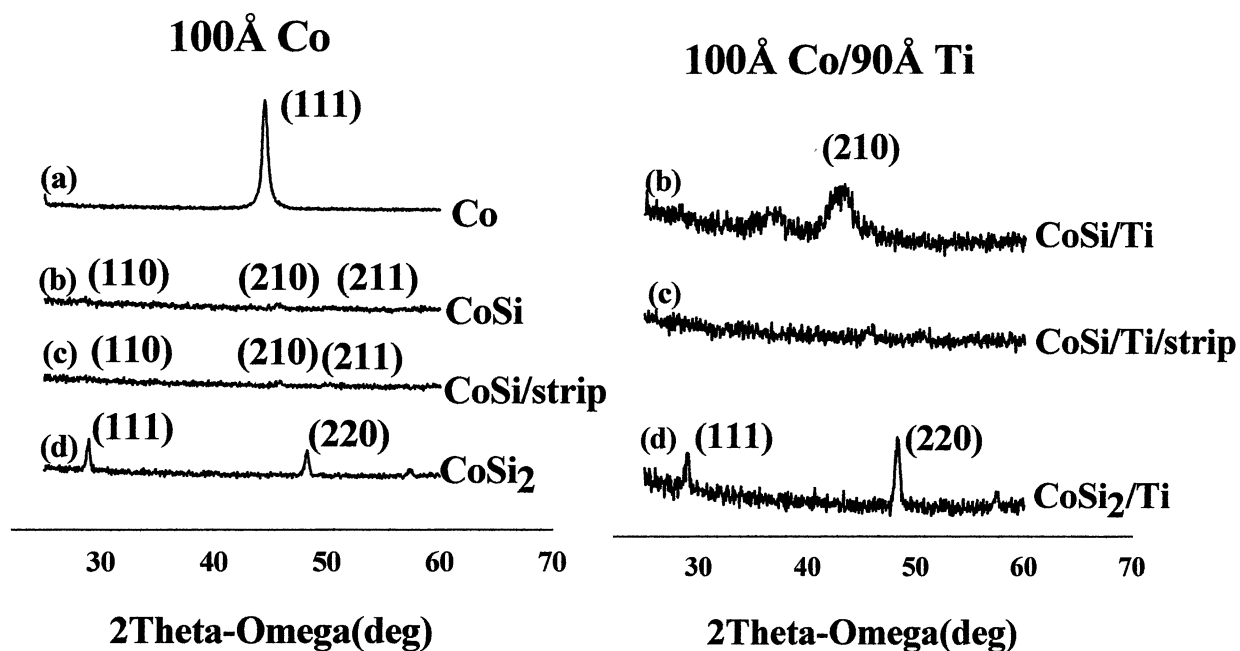


Figure 18: HAXRD scans for (a) as-deposited cobalt, (b) RTA1, (c) RTA1/strip, (d) RTA1/strip/RTA2. The scans show a highly ordered as-deposited cobalt film, and a tendency toward disorder after annealing as well as the formation of CoSi and CoSi₂ after the first and second anneal, respectively.

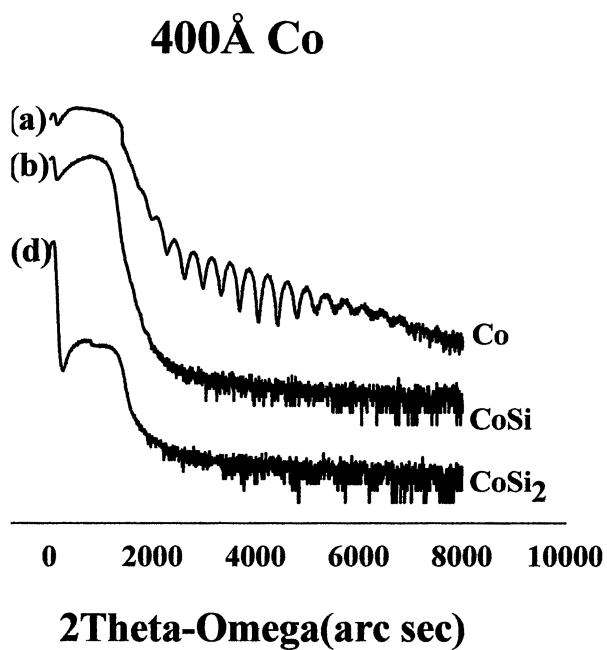
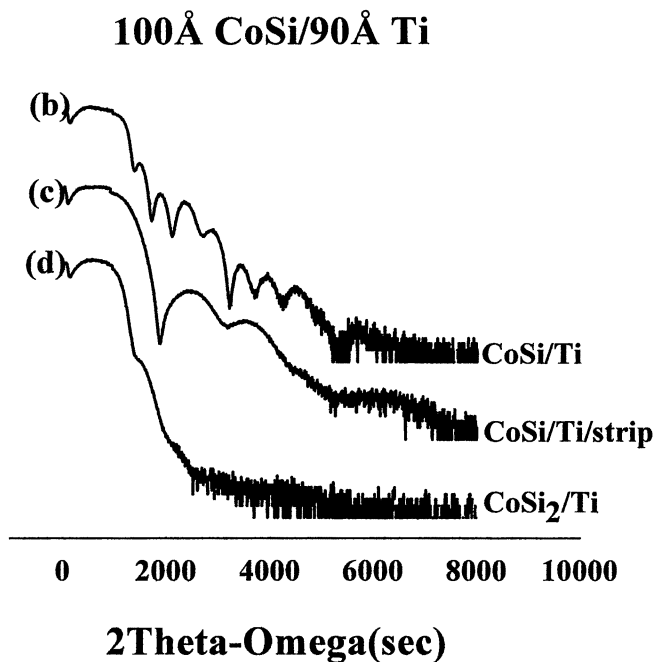
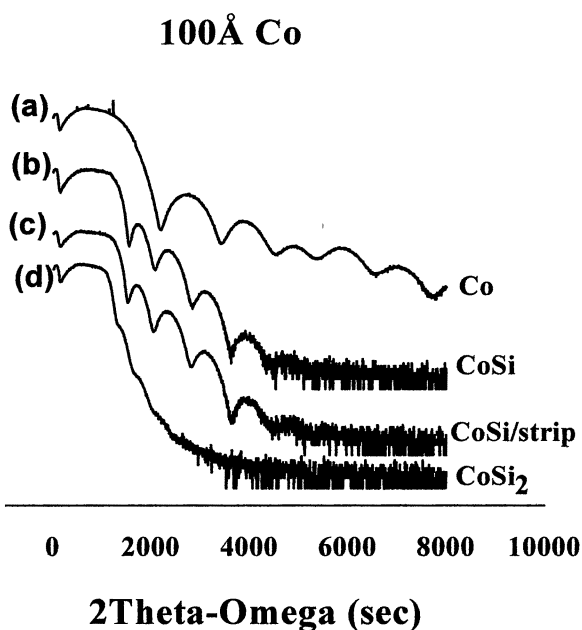


Figure 19: XRR scan for (a) as-deposited cobalt, (b) RTA1, (c) RTA1/strip, (d) RTA1/strip/RTA2. The scans show the roughness of the film increases with annealing as verified by AFM. The data fits also reveal the formation of CoSi and CoSi₂ after the first and second anneal, respectively.

3.2.3 REFS MERCURY DATA FITTING

Roughness (Å)	AFM	REFS
CoSi	11	14.9
CoSi/strip	10	14.8
CoSi ₂	46	35.8
CoSi/Ti	7	11.55
CoSi/Ti/strip	6	5.32
CoSi ₂ /Ti	37	27.7

Table 4: *Comparison of AFM vs. REFS computer modeling surface roughness*

The XRR data was then entered into a computer simulation program, REFS Mercury manufactured by Bede Scientific, Englewood, Colorado, and properties of the film were found by changing the parameters until an appropriate fit was made. The surface roughness obtained from the fit was then compared to the AFM data, as seen in Table 2. Note that the as-deposited cobalt did not undergo AFM measurements, and REFS analysis was not done for the 400 Å Co film since it is very rough and thick.

For thicker films, there are more fringes closer together, As the roughness of the film increases, the fringes become shallower. The data fits can be seen in Figs. 20. & 21.

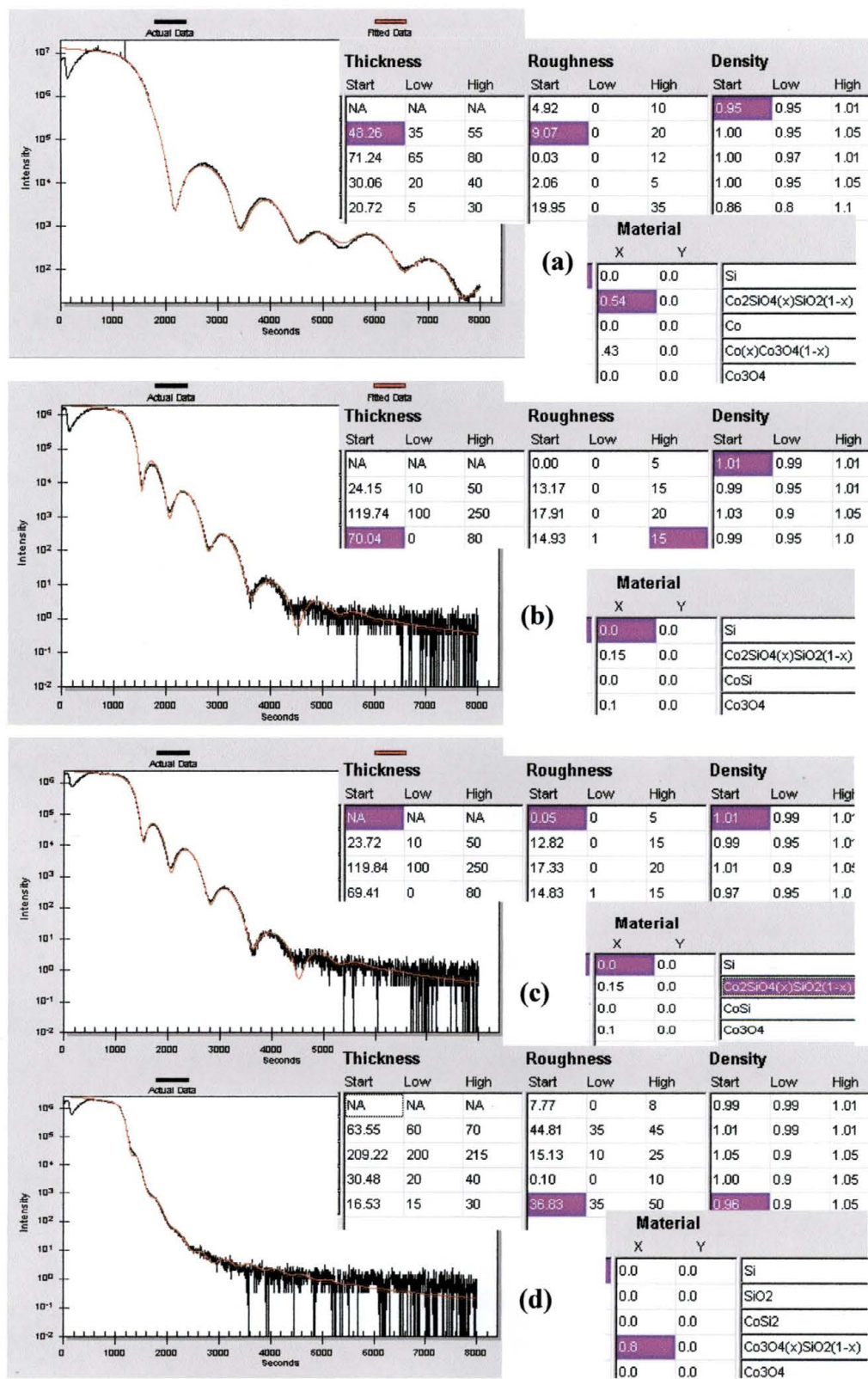


Figure 20: REFS computer modeling for 100Å Co (a) as-deposited Co, (b) RTA1, (c) RTA1/strip, (d) RTA2.

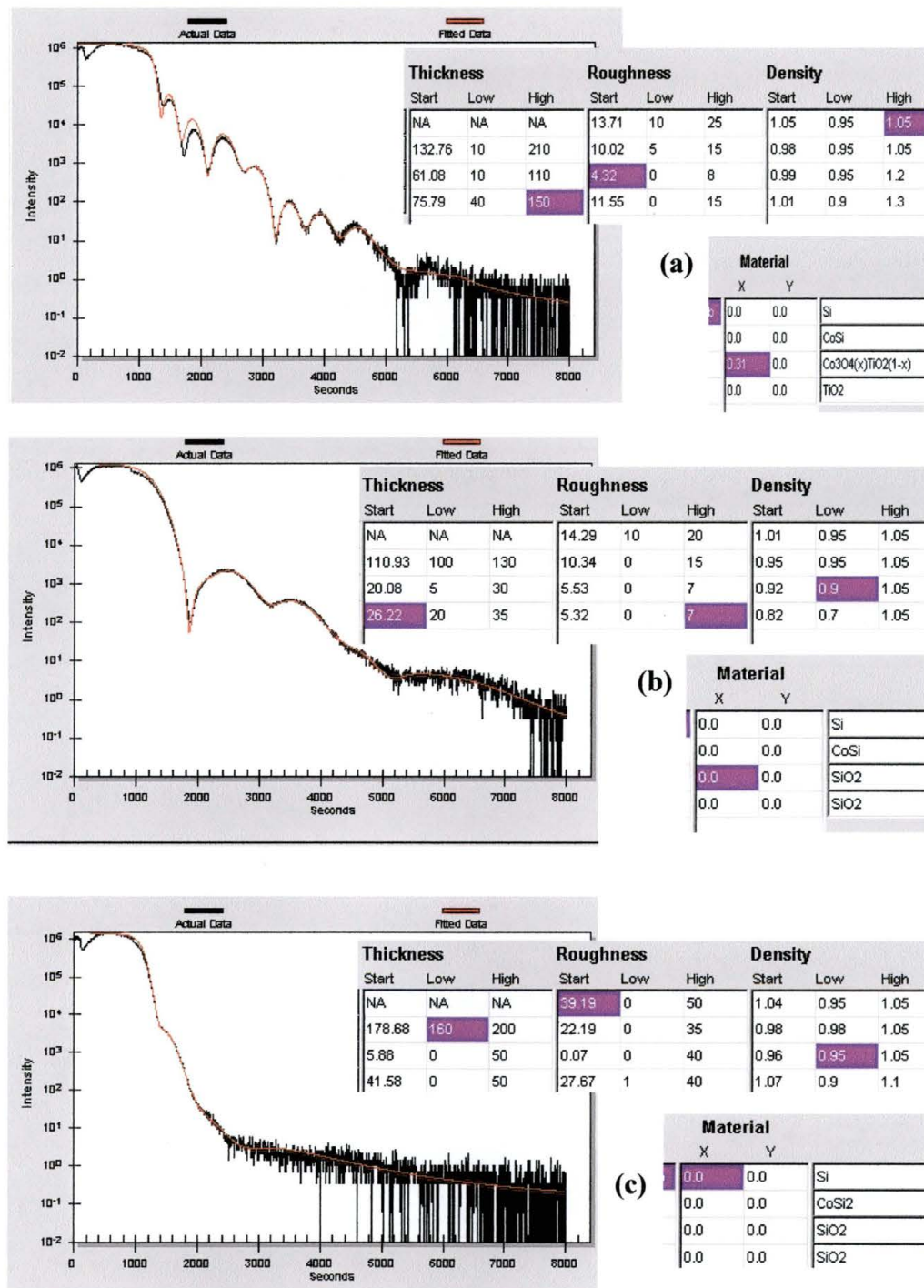


Figure 21: REFS computer modeling for $100\text{\AA}\text{Co}/90\text{\AA}\text{Ti}$ (a) RTA1, (b) RTA1/strip, (c) RTA2

3.2.4 VSM MEASUREMENTS

Another type of measurement done on the as-deposited cobalt film wafers was Vibrating Sample Magnetometry (VSM). The sample is placed between the poles of an electromagnet and caused to vibrate as the external magnetic field changes. The induced magnetic field of the sample will change until it reaches saturation in both directions. If the material is ferromagnetic it will have magnetization even when no magnetic field is applied. Otherwise, the VSM plot will show zero magnetic field in the absence of an applied field. For a more detailed explanation of VSM see previous thesis (Tijerina¹⁵).

The hysteresis VSM data in Fig. 22 shows the initial cobalt film to be ferromagnetic, as expected, since the magnetization of the field (y-axis) is not zero when the applied field (x-axis) is zero. The film after annealing shows no hysteresis and therefore no ferromagnetic properties at room temperature.

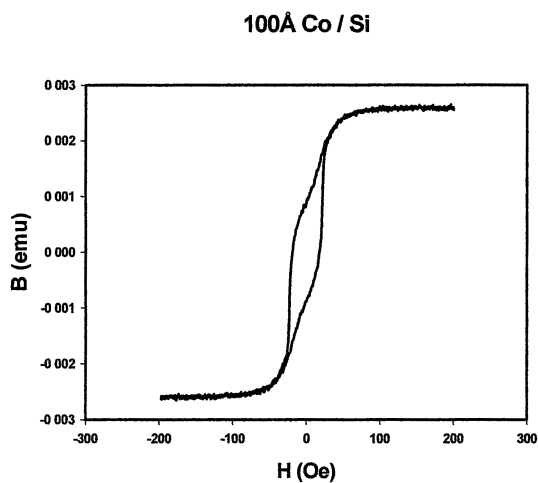
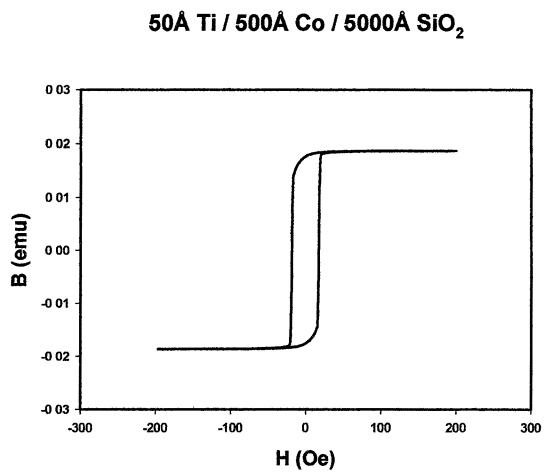
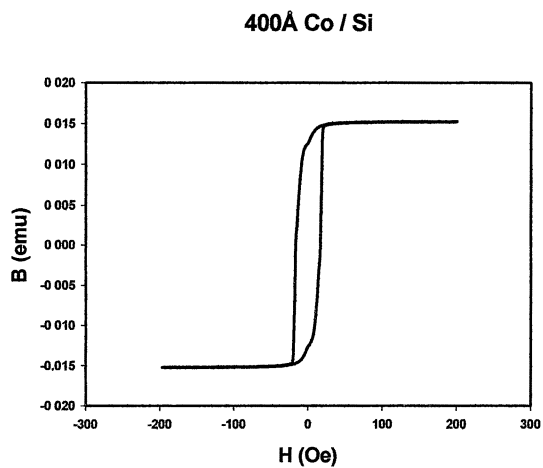


Figure 22: VSM data for 100 Å and 400 Å cobalt on silicon as well as 50 Å Ti/500 Å Co on 5000 Å Si; shows initial cobalt film to be ferromagnetic. After annealing, no hysteresis is seen (not shown).



CHAPTER 4

CONCLUSION

In conclusion, x-ray diffraction provides analysis for many properties of a material, both single crystal and amorphous. This is accomplished without damage to the material. This thesis showed the Williamson-Hall, Scherrer, and MudMaster (Fourier analysis) methods in order to evaluate size and strain properties of nanopowders to be an accurate method, especially when done in combination with TEM analysis. In the future, software will be purchased with the ability to determine the size distribution of particles analyzed with TEM. However, TEM analysis alone is not sufficient, since the small particles tend to agglomerate and statistics are difficult to extract.

Future research also includes fabrication of nanoparticles in the lab using a ball-milling machine. Powders of micron sizes are placed in a vial with a metal ball. The miller shakes the vial and the size of the powder decreases over milling time. These particles can then be studied to determine the relationship between size and milling time. Elemental diffraction can also be done to determine any structural changes in the crystal themselves. Crystallite size may be determined using MudMaster and compared to different milling times.

This thesis also supports the theory that Ti-capped Co produces a CoSi_2 film after annealing without impeding the silicidation process. HAXRD data shows fcc Co before annealing while PBXRD reveals the formation of CoSi after the first anneal and CoSi_2 after the second. The resulting film with Ti-capping is also free of an oxide layer at the

cobalt-silicon interface. This is not so without capping, as seen with the REFS Mercury fitting of XRR data.

This thesis has shown the usefulness of x-ray diffraction as a non-destructive method of determining properties of nanomaterials. Diffraction data in combination with other forms of analysis provide accurate descriptions of these materials. These tools are invaluable in aiding the advances of technology toward smaller, more reliable devices.

APPENDIX A

MudMaster Program

This program uses a Fourier analysis over one peak of x-ray diffraction data to calculate the average crystallite size of a material. A detailed description of using the MudMaster Program can be found in Eberl¹².

The basic steps are as follows:

1. Paste intensity data from diffraction analysis into column E of the sheet titled PeakPicker, beginning in row 2.
2. Specify the name of the sample in cells E1 and C4.
3. Give the step size of the measurement in cell B5.
4. In cell C6, enter the starting 2Theta value for the scan.
5. In cells C8 and C10, enter the 2Theta values for the start and end values, respectively, of the peak you want to analyze.
6. In cell C12, enter the reflection order of the peak, for instance, both 220 and 420 peaks enter 2.
7. In cell B20, enter the d-spacing which can be found from ICDD files.
8. Before running Peak Picker, it is important to click on an empty cell in all three sheets. If a cell with any value in it is highlighted, the program will not run.
9. Click "Start Peak Picker".
10. Peak Picker automatically enters peak information into Sheet 1 and the program immediately shows Sheet 2 which gives a volume weighted thickness of the crystallite size as well as the mean size.

	A	B	C	D	E
1	RESULTS				MgO36nm
2	PEAK MAXIMUM (TWO-THETA)		CLEAR COLUMN E, THEN PASTE INTENSITIES INTO E2:		227.34
3	42.59	STEP SIZE (deg. 2-theta; enter 0.02)	SAMPLE NAME		222.67
4	ANALYSIS RANGE (TWO-THETA)	0.095	MgO36nm		230.67
5	40.00	UPDATE SCREEN? (1 = yes; enter 0)	START ANGLE FOR ALL INTENSITIES		242.34
6	45.17	0	30.04635		230.34
7	MAXIMUM INTENSITY OF PEAK	PLOT PATTERN? (1 = yes; enter 1)	ACT START ANGLE FOR ANALYSIS		241.67
8	2926.7	1	40		220.01
9	ANGLES FOR TAIL MINIMUMS	PICK SYMM PEAK? (1 = yes; enter 0)	END ANGLE FOR ANALYSIS		238.34
10	40.69	1	45		219.01
11	44.77	WAVELENGTH COR.? (1 = yes; see cells G)	REFLECTION ORDER		231.01
12	INTENSITIES FOR TAIL MINIMUMS	0	2		214.01
13	222.9	PLOT PATTERN? (0 = no; or 1, 2, 3 or 4; enter 1)	ANAL. STRAIN? (0 = no; 1-5 = anal. no.)		214.34
14	172.5	2	0		215.34
15	APPROXIMATE THICKNESS (nm)		AUTOPASTE?		229.34
16	9.5	CALC APPROX MEAN? (0 = no; 1 = DSE; 2 = lognorm; 3 = lognorm; 4 = PVP; 5 = illite max/bg; enter 1)	(0 = no; 1 = paste; 2 = start)		214.34
17	AVERAGE PEAK BREADTH (DEGREES 2-THETA)	3	2		222.01
18	0.71	d 001 (Å; for approx thick calc)			217.01
19	INTEGRATED INTENSITY		START PeakPicker		220.67
20	1880.7	2.106	U.S. Geological Survey		213.67

	A	B	D	H
1	SAMPLE NAME	DIST. LIMIT? (nm)	YM. STRAIN COR.? (1=YES)	NO LpG² CORRECTION
2	MgO36nm	18	1	BEST MEAN (nm; EXTRAPOLATED; area-weighted; se
3	OF MM ANAL. 1 = least sq.; 0 = no; 1 = mov		INST COR? (1 = YES)	9.5
4	12/9/2003 7:37	0	1	MEAN (nm; DISTRIBUTION; area-weighted)
5				8.7
6				ALPHA (from nm)
7				2.06
8				BETA ²
9				0.22
10				VOL-WEIGHTED MEAN THICKNESS (nm)
11				10.4
12				POSITION INT. FN. (two-theta)
13				42.66
14				d-SPACING INT. FN. (Å)
15				2.118
16				ROOT MEAN SQUARE STRAIN (Å; see cells L11
17				Not calculated
18				APPROX FUND PART THICK (nm; area-weight
19				Not applicable
20				ILLITE FIXED CATIONS/HALF-UNIT CELL (see L

Thickness (Area-weighted frequency)

MgO36nm

Extrapolated Mean

PeakPicker Sheet1 Sheet2

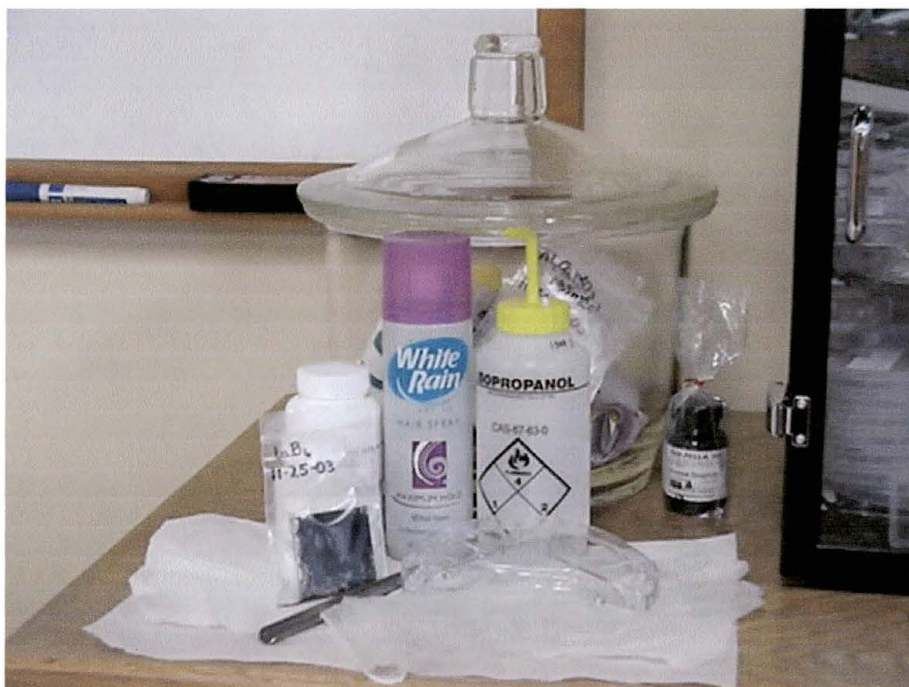
APPENDIX B

NANOPOWDER PREPARATION

XRD Analysis

Nanopowders should always be kept in a desiccator to prevent the powder from reacting with air or water. The fastest and most efficient method of preparing powder samples for XRD analysis is as follows:

1. Wear gloves and safety goggles, since not much is known about the hazards of nano-sized powders.
2. Spray a two-inch square glass slide with hairspray. White Rain Maximum Hold was used effectively.
3. Quickly spread powder over the hairspray before it dries. A thin layer, just enough to cover the slide, is sufficient.
4. Shake off any excess powder then spray again, essentially sandwiching the powder between two layers of hairspray.
5. Position the slide in the center of the sample holder.
6. The slide can be reused and can be stored in small, sealable plastic bags which should be kept in a desiccator. Be sure to label the bags according to material, size, and date.



TEM Analysis

Nanopowders can be prepared for TEM analysis as follows:

1. 200 square copper grids were used, as opposed to 100 because this means the squares are smaller (more fit into a grid) and creates better support for the Formvar® film.
2. Drop a solution 0.25 % or 0.5 % polyvinyl formal (Formvar®) in ethylene dichloride or chloroform onto a water surface with a glass pipette.
3. The solution floats on the water and the grids can then be placed on the solution, dull side down.
4. Scoop the grids out with paper. Paper can be a strip of index card sliced with a razor.
5. Place the grids in a petri dish on filter paper and allow to dry.
6. Sonicate the nanopowder for twenty minutes in deionized water and place small droplets of the solution on the grids with a syringe and allowed to dry.



BIBLIOGRAPHY

-
- ¹ L.J. De Jongh, Electronic Properties of Metalcluster Compounds: Nanophase Materials from Chemical Synthesis, *Nanophase Materials*, 1994, pp. 349.
- ² <http://jan.ucc.nau.edu/~wittke/Microprobe/Xray-NamingTransitions.html>.
- ³ R. Jenkins, R.L. Snyder, *Introduction to X-Ray Powder Diffractometry*, Wiley-Interscience, 1996.
- ⁴ B.D. Cullity, *Elements of X-Ray Diffraction, 3rd Edition*, Addison-Wesley Publishing Co., Massachusetts, 2001.
- ⁵ <http://biophysics.med.jhu.edu/courses/pdf/2002/xrayp3.pdf>.
- ⁶ M. Schuster, H. Göbel, Parallel-Beam Coupling into Channel-cut Monochromators Using Curved Graded Multilayers, *Journal of Physics D; Applied Physics*, Vol. 28, 1995, pp. A270-A275.
- ⁷ J. P. Gambino, E. G. Colgan, Silicide and Ohmic Contacts, *Materials Chemistry and Physics*, Vol. 52, 1998, pp. 99-146.
- ⁸ http://www.basf.de/en/ueber/dienste/wfw/einsatz/titan.htm?id=V00-*E3X9k-**bsf800.
- ⁹ R.A. Roy, C. Cabral, Jr., C. Lavoie, The Future of Silicides for CMOS Contacts, *Materials Research Society Symposium Proceedings*, Vol. 564, 1999, pp. 35-45.
- ¹⁰ C. Detavernier, R.L. Van Meirhaeghe, F. Cardon, R.A. Donaton, K. Maex, The Influence of Ti Capping Layers on CoSi₂ Formation, *Microelectronic Engineering*, Vol. 50, 2000, pp. 126-132.
- ¹¹ http://www.appt-powders.com/mcp_advantages.htm.
- ¹² D.D. Eberl, V.A. Drits, J. Srodon, R. Nüesch, MudMaster: A Program for Calculating Crystallite Size Distributions and Strain from the Shapes of X-Ray Diffraction Peaks, US Geological Survey, Open-File Report 96-171, 1996, www.geol.uni-erlangen.de/html/software/mudmaster.html.
- ¹³ J.R. Koke, Cytology and Microtechnique, lecture notes, <http://www.bio.txstate.edu/%7ejrkoke/cytology/CM-lectures/4-MicroII.pdf>, 2003.
- ¹⁴ K.E. Sickafus, TEM Transmission Electron Microscopy, *Encyclopedia of Materials Characterization*, Butterworth-Heinemann, Massachusetts, 1992.

¹⁵ A. Tijerna, *Investigations into Non-Conventional Materials for High-K Dielectrics and the Unique Production of Permalloy Oxides for GMR Devices*, Master's Thesis, Southwest Texas State University, 2002.

¹⁶ A. Ayala, *Advanced X-ray characterization of ULSI materials*, Master's Thesis, Southwest Texas State University, 2000.

¹⁷ A.R. Ivanova, G. Nuesca, X. Chen, C. Goldberg, A.E. Kaloyeros, B. Arkles, J.J. Sullivan, The Effects of Processing Parameters in the Chemical Vapor Deposition of Cobalt from Cobalt Tricarbonyl Nitrosyl, *Journal of the Electrochemical Society*, Vol. 146, 1999, pp. 2139-2145.

VITA

Shannon Gail Fritz was born in San Antonio, Texas, on November 24, 1978, the daughter of Judith Lynn Fritz and William Robert Fritz. After completing her work at East Central High School, San Antonio, Texas, in 1997, she entered Texas Lutheran University, Seguin, Texas. She received the degree of Bachelor of Arts for Physics in the spring of 2001. In the summer of the same year, she entered the Graduate School of Texas State University where she worked as both a research and teaching assistant.

Upon completion of the degree of Master of Science for Physics, Shannon will begin doctoral studies at University of Nebraska, Lincoln. Her research will focus on magnetic nanoparticles for biomedical applications.

PRESENTATIONS and PAPERS

(1) "The Influence of Rapid Thermal Annealing and Chemical Treatment Methods on the Crystallinity and Morphology of Sputtered Co and Co Silicide Films", APS March Meeting 2003 [Y7.004], Shannon Fritz (presenter)

(2) "The Structural and Magnetic Characterization of Cobalt Silicide Films Formed by Rapid Thermal Annealing", Spring Meeting of the Texas Sections of the APS, March 2002, Shannon Fritz (presenter)

"The Ion Beam Sputter-Fabrication of Bi-YIG Films for Magnetic Photonic Applications", submitted to IEEE Transactions in Magnetics, in review

"A Comparison of X-ray and Scanning Probe Characterization of Cobalt Silicidation", to be submitted to the Journal of Vacuum Science and Technology B

Permanent Address: 601 University Dr.
San Marcos, TX 78666

This thesis was typed by Shannon G. Fritz.